Journal of Cerebral Blood Flow & Metabolism (2012), 1–33

www.jcbfm.com

Review Article

Two-photon microscopy as a tool to study blood flow and neurovascular coupling in the rodent brain

Andy Y Shih[1], Jonathan D Driscoll[1], Patrick J Drew[2,3], Nozomi Nishimura[4], Chris B Schaffer[4] and David Kleinfeld[1,5]

[1]*Department of Physics, University of California at San Diego, La Jolla, California, USA;* [2]*Department of Engineering Science and Mechanics, Pennsylvania State University, University Park, Pennsylvania, USA;* [3]*Department of Neurosurgery, Pennsylvania State University, University Park, Pennsylvania, USA;* [4]*Department of Biomedical Engineering, Cornell University, Ithaca, New York, USA;* [5]*Section of Neurobiology, University of California at San Diego, La Jolla, California, USA*

The cerebral vascular system services the constant demand for energy during neuronal activity in the brain. Attempts to delineate the logic of neurovascular coupling have been greatly aided by the advent of two-photon laser scanning microscopy to image both blood flow and the activity of individual cells below the surface of the brain. Here we provide a technical guide to imaging cerebral blood flow in rodents. We describe in detail the surgical procedures required to generate cranial windows for optical access to the cortex of both rats and mice and the use of two-photon microscopy to accurately measure blood flow in individual cortical vessels concurrent with local cellular activity. We further provide examples on how these techniques can be applied to the study of local blood flow regulation and vascular pathologies such as small-scale stroke.
Journal of Cerebral Blood Flow & Metabolism advance online publication, 1 February 2012; doi:10.1038/jcbfm.2011.196

Keywords: blood flow; cranial window; neurovascular coupling; stroke; two-photon microscopy; vasculature

Introduction

The brain uses more energy than any other organ of the body and relies almost exclusively on moment-to-moment delivery of glucose and oxygen (O_2) through the blood. Roy and Sherington (1890), on observing that an increase in neuronal activity caused a local rush of blood into the brain, proposed that neural activity and blood flow were linked. They further postulated that the flow increase existed as a mechanism to support the metabolic demand of active neurons. Our understanding of this phenomenon, commonly termed functional hyperemia or neurovascular coupling, remains an active area of research (Attwell *et al*, 2010). However, recent studies have highlighted important conditions under which neural activity and blood flow become decoupled (Devor *et al*, 2008; Jukovskaya *et al*, 2011; Sirotin and Das, 2008), and thus raise basic questions about neurovascular coupling (Kleinfeld *et al*, 2011). One set of questions concerns the patterns of neuronal signals that lead to vasoactivity. In particular, what classes of inhibitory vs. excitatory cells have a dominant role and how are their synaptic events converted into dilatory vs. constrictive responses in blood vessels? A second set concerns the role of astrocytes that ensheath the vasculature. In particular, are they intermediary cells that deliver signals from neuron to vasculature (Zonta *et al*, 2003) or do neuronal signals have a direct effect on blood vessels (Cauli *et al*, 2004)? A final question set concerns how mechanisms of neurovascular coupling change in response to diseases of the nervous system (Girouard and Iadecola,

Correspondence: Professor D Kleinfeld, Department of Physics, University of California at San Diego, 9500 Gilman Drive, La Jolla, CA 92093-0374, USA.
E-mail: dk@physics.ucsd.edu
This work was supported by the American Heart Association (Post-doctoral fellowship to AYS and 0735644T to CBS), the Ellison Medical Foundation (AGNS033006 to CBS), the L'Oréal USA Fellowship for Women in Science (to NN), and the National Institutes of Health (MH085499, EB003832, and OD006831 to DK and AG031620 to NN).
Received 23 June 2011; revised 18 October 2011; accepted 13 November 2011

2006). In particular, how do the circuits that regulate blood flow break down during stroke and other vascular pathologies. Further, are there mechanisms that can replenish their function after injury?

Techniques to measure blood flow and vascular tone are essential if we are to delimit neurovascular coupling in health and disease. What are the spatial scales that govern these measurements? Although the mouse brain is some 10 mm in extent (Figure 1A), blood flow data is typically analyzed within a cortical column, a region of nominally uniform neuronal activation that extends the full depth of the gray matter (Figure 1B). This corresponds to a cylinder of tissue roughly a few hundred micrometers in diameter and 1 mm in depth in mouse. Single penetrating arterioles, which have the key role of transporting blood from the cortical surface to the subsurface microvasculature, control flow to a similar volume of tissue (Figure 1B) (Bar, 1980). Thus, perfusion changes in a single penetrating vessel can directly impact flow to localized beds of underlying microvessels (Nishimura *et al*, 2007).

If we consider the flow through a single penetrating arteriole as a single unit of cortical perfusion (Woolsey *et al*, 1996), how are the spatially and temporally rich patterns of cortical blood flow generated? On the spatial scale of millimeters, flow through tens to hundreds of penetrating arterioles is orchestrated by global control mechanisms, which include the activity of subcortical and brainstem nuclei that project broadly onto the cells and/or vasculature of cortex (Drew *et al*, 2008; Golanov *et al*, 2000; Hamel, 2006), cortical gamma rhythms (Niessing *et al*, 2005; Nir *et al*, 2008), and intrinsic oscillations in the calcium ion concentration ($[Ca^{2+}]_{int}$) in vascular smooth muscle (Filosa *et al*, 2004).

Blood flow regulation on the spatial scale of 1 to 100 μm acts on subsurface vascular segments, which are smaller than a single penetrating arteriole unit. For example, locally active neurons and ensheathing astrocytes may release vasoactive molecules onto a subsurface arteriolar branch (Attwell *et al*, 2010), or the constriction of pericytes may affect flow at the junction of a single capillary branch (Fernández-Klett *et al*, 2010; Peppiatt *et al*, 2006). How do these small

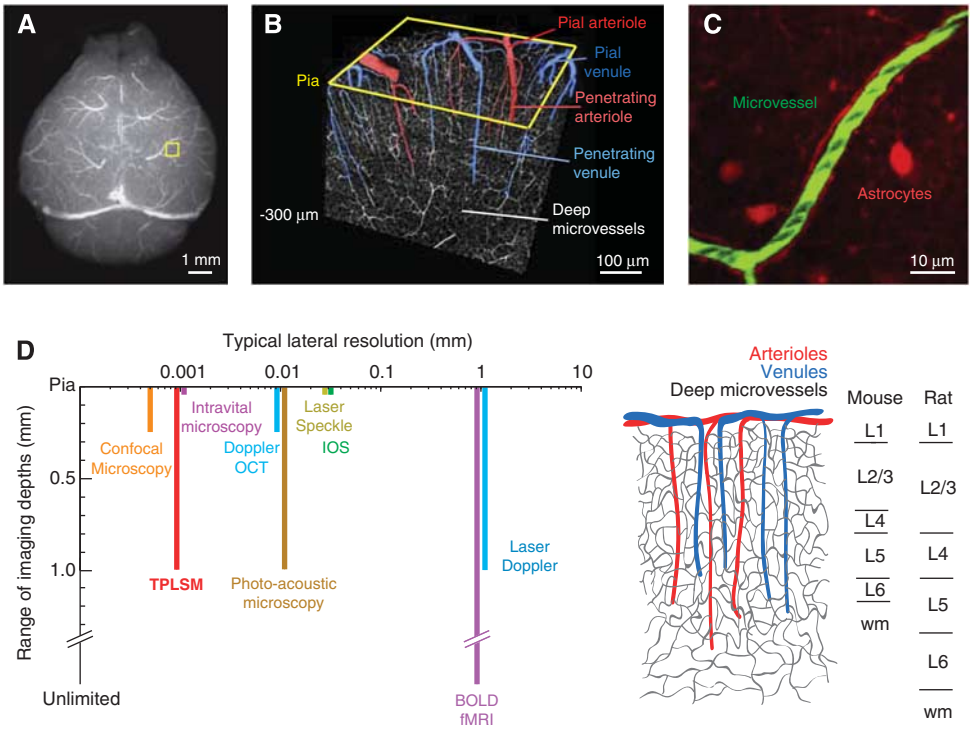

Figure 1 Imaging the microarchitecture of the rodent cerebral vasculature. (**A**) Wide-field epi-fluorescence image of a C57Bl/6 mouse brain perfused with a fluorescein-conjugated gel and extracted from the skull (Tsai *et al*, 2009). Pial vessels are visible on the dorsal surface, although some surface vessels, particularly those that were immediately contiguous to the sagittal sinus, were lost during the brain extraction process. (**B**) Three-dimensional reconstruction of a block of tissue collected by *in vivo* two-photon laser scanning microscopy (TPLSM) from the upper layers of mouse cortex. Penetrating vessels plunge into the depth of the cortex, bridging flow from surface vascular networks to capillary beds. (**C**) *In vivo* image of a cortical capillary, 200 μm below the pial surface, collected using TPLSM through a cranial window in a rat. The blood serum (green) was labeled by intravenous injection with fluorescein-dextran conjugate (Table 2) and astrocytes (red) were labeled by topical application of SR101 (Nimmerjahn *et al*, 2004). (**D**) A plot of lateral imaging resolution vs. range of depths accessible for common *in vivo* blood flow imaging techniques. The panels to the right show a cartoon of cortical angioarchitecture for mouse, and cortical layers for mouse and rat in relation to imaging depth. BOLD fMRI, blood-oxygenation level-dependent functional magnetic resonance imaging.

changes affect flow in the cerebral vasculature and how do they operate within the sea of ongoing globally controlled vasoactivity? Understanding this relationship requires methods that can image at the resolution of individual cells, microvessels, and fine cellular processes, i.e., down to voxels $<1\,\mu m^3$ (Figure 1C).

Choice of Tools

There is no one tool that can measure from the scale of microvessels to the entire cortical mantle (Figure 1D). The goal of this review is to show that rigorous methods do exist to study blood flow at the micrometer to millimeter spatial scales of vascular function and regulation, i.e., single penetrating vessels and their subsurface branches.

Setting aside the need to image below the pial surface, intravital microscopy, in which the pial surface is imaged at high frame rates, can be used to observe single pial vessels (Ngai *et al*, 1988). This technique is capable of extracting changes in vessel diameter (Ko *et al*, 1990; Morii *et al*, 1986). Concomitant changes in red blood cell (RBC) speed can be collected by intravenous injection of RBCs that have been exogenously labeled with a fluorescent dye (Rovainen *et al*, 1993; Woolsey *et al*, 1996). Plasma velocity can be measured by tracking small fluorescent beads that are intravenously injected (Rovainen *et al*, 1993). However, imaging is restricted to vessels on or close to the pial surface. Thus, diameter changes in subsurface penetrating vessels and microvessels, which are critical for neurovascular coupling, cannot be examined.

Full-field imaging techniques other than intravital microscopy, including intrinsic optical imaging (Frostig *et al*, 1990; Grinvald *et al*, 1986) and laser speckle imaging (Dunn *et al*, 2001), yield information about changes in blood oxygenation and/or blood flow, but are inappropriate for measuring flow below the cortical surface at high resolution. Laser Doppler imaging measures flow deep to the brain surface but also suffers from low spatial resolution (Ances *et al*, 1999). Blood-oxygenation level-dependent functional magnetic resonance imaging (BOLD fMRI) has no restriction to the depth of imaging, but temporal and spatial resolution are also low (Ogawa *et al*, 1992). Emerging techniques such as optical coherence tomography (Srinivasan *et al*, 2009, 2011), photoacoustic microscopy (Hu and Wang, 2010), and functional ultrasound imaging (Mace *et al*, 2011) are gaining the capacity to resolve flow in large numbers of individual vessels in cortex and may be able to address issues regarding global flow regulation. Critically, none of these methods currently combine imaging of blood flow and cellular activity at high resolution, and are thus less appropriate for studies seeking to link cellular activity with blood flow.

The use of confocal laser-scanning microscopy improves the ability to measure flow in single vessels concurrent with indicators of cellular activity below the pial surface. Here, the vascular serum is labeled with a fluorescent dye to visualize the whole vessel lumen. The dye is conjugated to a high-molecular-weight dextran to prevent its leakage from the vasculature. Non-fluorescent RBCs are then tracked on this fluorescent background (Dirnagl *et al*, 1989). The optical sectioning capabilities of this method allow imaging of subsurface vessels down to $\sim 100\,\mu m$ below the surface. However, imaging of neuronal populations generally requires greater depth penetration, i.e., 300 to $500\,\mu m$ below the surface. This problem is alleviated by two-photon laser scanning microscopy (TPLSM; Denk *et al*, 1990), an optical sectioning technique in which absorption of light to excite fluorescent molecules occurs only at the laser focus. Two-photon laser scanning microscopy offers two critical advantages over confocal microscopy: (i) deeper imaging with longer wavelength excitation; and (ii) reduced photodamage and photobleaching of dyes caused by out of focus excitation (Helmchen and Denk, 2005; Kobat *et al*, 2009).

We suggest that TPLSM is the method of choice for the imaging of blood flow (Driscoll *et al*, 2011*a*; Helmchen and Kleinfeld, 2008; Kleinfeld *et al*, 1998, 2008; Kleinfeld, 2002; Shih *et al*, 2009; Tiret *et al*, 2009). Past studies have made use of TPLSM to examine vascular dynamics in somatosensory cortex (Blinder *et al*, 2010; Brown *et al*, 2007; Devor *et al*, 2007, 2008; Drew *et al*, 2011; Fernández-Klett *et al*, 2010; Hutchinson *et al*, 2006; Kleinfeld *et al*, 1998; McCaslin *et al*, 2010; Nishimura *et al*, 2007, 2010; Schaffer *et al*, 2006; Shih *et al*, 2009; Sigler *et al*, 2009; Stefanovic *et al*, 2007; Tian *et al*, 2010; Wang *et al*, 2006; Winship *et al*, 2007; Zhang *et al*, 2005; Zhang and Murphy, 2007) and the olfactory bulb (Chaigneau *et al*, 2003, 2007; Jukovskaya *et al*, 2011; Lecoq *et al*, 2009; Petzold *et al*, 2008). Recent advancements show that TPLSM can allow single microvessels to be studied throughout the full depth of cortex (Kobat *et al*, 2009), which is important as vascular regulation appears to initiate in middle and deeper layers of cortex (Tian *et al*, 2010). A further advantage is the ability to use of fluorescent-based functional reporters or endogenous signals to record cellular activity, such as changes in $[Ca^{2+}]_{int}$ (Chaigneau *et al*, 2007; Petzold *et al*, 2008; Wang *et al*, 2006), and the ratio of $[NADP]_{int}$ to $[NAD^+]_{int}$ (Kasischke *et al*, 2011; Murphy *et al*, 2008*b*) concurrent with blood flow and vessel diameter changes. Last, TPLSM may be used to image subsurface vasodynamics through a chronic window in awake mice (Drew *et al*, 2010*b*, 2011).

How Can Two-Photon Laser-Scanning Microscopy Help Delimit the Logic of Neurovascular Coupling?

Neurovascular coupling is thought to occur locally, through a complex interplay of signaling cascades among neuronal processes and astroglial endfeet that surround the vascular wall (Attwell *et al*, 2010; Iadecola and Nedergaard, 2007). The hemodynamic

response is dominated by arteriole dilation at the center of the response, where neural activity is most pronounced (Derdikman *et al*, 2003; Devor *et al*, 2008), whereas the surrounding regions are dominated by delayed arteriole constrictions that lead to an overall decrease in flow (Devor *et al*, 2008). What signals generate this spatiotemporal pattern of blood flow? Although multiple vasoactive pathways have been identified, their roles in generating a hemodynamic response remain unclear (Attwell *et al*, 2010; Kleinfeld *et al*, 2011). Two-photon imaging, which has been used with great rigor in slice experiments (Gordon *et al*, 2008; Mulligan and MacVicar, 2004), can meet the necessary challenges to dissect these pathways *in vivo*. First, a link between neuronal and astrocytic activity and local vasodynamics can be verified. For example, activity in astrocyte endfeet can be measured in relation to the flow speed and diameter changes in neighboring as well as distant blood vessels (Takano *et al*, 2006; Winship *et al*, 2007). Second, the cellular specificity of a manipulation, whether pharmacologically or genetically targeted, can be verified visually. Third, techniques used to activate or record from single cell types, such as single-cell electrophysiology (Gentet *et al*, 2010) or optical uncaging of intracellular Ca^{2+} (Takano *et al*, 2006), can be visually guided. Finally, the activity in many cells can be correlated with the response in multiple neighboring vessels to facilitate a shift away from 'single cell and single vessel' studies. Future efforts will likely be placed on examining neuronal networks within a cortical column and the flow changes in vessel segments throughout the vascular tree that feeds the column.

An additional line of research that stands to gain from TPLSM is the basis of dysfunction or blockade of a single microvessel and its relation to cortical pathology. A significant proportion of human stroke cases involve obstruction of small cerebral vessels, possibly leading to microinfarctions (Das *et al*, 2008). The accumulation of multiple small strokes during atherosclerosis or amyloid angiopathy may lead to long-lasting deficits in function and cognition, as seen with different forms of dementia (Gold *et al*, 2007; Suter *et al*, 2002). Rodent models to study the consequences of small vessel disease (Hainsworth and Markus, 2008) require measurement and manipulation of flow in single vessels, both at the pial surface (Blinder *et al*, 2010; Nguyen *et al*, 2011; Nishimura *et al*, 2007, 2010; Schaffer *et al*, 2006) and in subsurface microvessels (Nishimura *et al*, 2006). Of particular importance is the use of chronic preparations where the consequences of vascular obstruction can be studied longitudinally (Drew *et al*, 2010*b*).

Focus of this Review

Here, we provide details on how to perform single- and multivessel TPLSM imaging of blood flow dynamics, concurrent with cellular activity, in the somatosensory cortex of anesthetized and awake rodents. First, we compare advantages and disadvantages of using rat and mouse species for blood flow imaging studies. Second, we describe the surgical tools and procedures used to generate acute and chronic cranial windows; video resources for chronic imaging windows are available (Marker *et al*, 2010; Shih *et al*, 2012). Third, we discuss how blood flow imaging data are collected using TPLSM and the calculation of relevant flow parameters from single cerebral vessels. Finally, we provide case studies on how auxiliary lasers and cell-labeling techniques can be used to address critical questions concerning neurovascular function in health and disease. The equipment and algorithms used in these studies have been summarized elsewhere, including basic hardware (Driscoll *et al*, 2011*b*; Tsai and Kleinfeld, 2009) and software (Nguyen *et al*, 2006, 2009) for TPLSM, and algorithms for data analysis (Drew *et al*, 2010*a*; Driscoll *et al*, 2011*a*; Kleinfeld and Mitra, 2011; Valmianski *et al*, 2010). Additional work has addressed the use of TPLSM to image histological tissue with labeled vasculature (Kleinfeld *et al*, 2011; Ragan *et al*, 2007; Tsai *et al*, 2003, 2009, 2011).

Methodological overview

Mouse vs. Rat and Chronic vs. Acute Preparations

Both rats and mice have their place in cerebral blood flow imaging studies. It is important to choose the model species based on the goal of the experiment. Rats, for example, are larger animals and thus preferred for complex surgical procedures. Cranial windows can be made large to allow access to multiple regions of cortex and physiological parameters can be more easily controlled. However, a major disadvantage is that imaging quality of rat cranial windows tend to degrade within days. In contrast, mice are excellent for repeated imaging studies as transcranial windows with a thinned skull are generally stable for months. The use of mice allows researchers to exploit a wide range of vascular-related transgenics that now exist. However, physiological parameters are more difficult to control with anesthetized mice.

Physiological Variables

An important factor for blood flow imaging in anesthetized rodents is the maintenance of levels of blood gas, blood pressure, and body temperature within an accepted physiological range. Deviations from the normal physiological state leads to abnormal vascular dynamics. Simply maintaining stable anesthesia is often insufficient as prolonged periods of anesthesia lead to an increase in the partial pressure of carbon dioxide (pCO_2) in the blood and a decrease in blood pressure, which in turn lead to gradual vasodilation (Lassen and Christenson, 1976).

Rats, because of their larger size, allow for the best control of physiological variables as arterial and venule catheters are easier to place and more blood can be drawn for intermittent monitoring of blood gas (Waynforth and Flecknell, 1992). A femoral artery catheter also serves as a means to continuously monitor blood pressure via an attached pressure transducer. The alternative is to use a pressure cuff transducer, which is noninvasive but permits only intermittent measurements.

Assessment of physiological variables in mice requires more surgical skill than for rats. An important consideration is that the total amount of blood for a 30 g mouse is only $\sim$2.4 mL (Harkness and Wagner, 1989), and each withdrawal of blood for measurement in a conventional blood-gas monitor will reduce blood volume by $\sim$4% (McGuill and Rowan, 1989). Repeated sampling of blood over a short period of time would undoubtedly alter vasodynamics. Thus, blood-gas machines that read smaller blood samples, e.g., $<100\,\mu$L per sample, are better suited for mouse studies (Bayer RapidLab, Norwood, MA, USA; 248 can work with 60 μL blood samples). An alternative method is to monitor the buildup of pCO_2 in the expired air (microCapStar End-Tidal CO_2 Analyzer, CWE Inc., Ardmore, PA, USA) to gauge respiratory status and depth of anesthesia, although absolute measures of blood pO_2, pCO_2, pH, [glucose], etc. are more informative of the physiological state. Artificial ventilation is an invasive but effective means to maintain blood gas levels for extended imaging periods in acute studies (Moldestad *et al*, 2009). Finally, pulse oximeters are noninvasive and should be used routinely to gauge the O_2 saturation of hemoglobin in the blood as well as heart and breathing rate for both rats and mice.

Two-photon imaging studies of rodents are rapidly moving toward the use of behaving animals (Dombeck *et al*, 2007; Greenberg *et al*, 2008; Sawinski *et al*, 2009), including studies of blood flow (Drew *et al*, 2011), and the determination of physiological variables will also prove to be critical. Fluctuations in blood pressure may occur during heightened stress or physical activity, and will influence cerebral blood flow. To measure such changes chronically in awake imaging studies, indwelling and remotely transmitted monitors for blood pressure could be used for some experiments (Butz and Davisson, 2001). Although technically very challenging in mouse, chronically implanted arterial and venule catheters enable researchers to draw blood and deliver drugs without added stress to the animal. Finally, implanted wire electrodes to collect ongoing electrocorticograms and electrocardiograms allow noninvasive monitoring of brain state and heart rate, respectively (Pinnacle Technology Inc., Lawrence, KS, USA).

The main advantage of an acute anesthetized preparation is that it allows rigorous physiology monitoring. Blood gas and pressure can be 'tuned' to a normal physiological state by adjusting anesthesia and the use of pharmacological agents. In contrast, chronic imaging preparations will almost always be less physiologically controlled as many methods for physiological monitoring are too invasive for survival studies. Yet chronic imaging of awake animals obviates concerns regarding homeostasis, particularly suppressed autoregulation of the vascular supply caused by anesthetics (Hoffman *et al*, 1991).

Cranial Windows

The generation of a cranial window for optical access in rats and mice differ on a number of levels. In rats, the overlying bone must be completely removed. Further, the dura mater must be carefully resected to the edge of the imaging window for TPLSM (Kleinfeld and Delaney, 1996; Levasseur *et al*, 1975; Morii *et al*, 1986). The window must then be resealed to restore intracranial pressure and to minimize motion artifacts caused by heart beat and breathing (Figure 2). The clarity through such a cranial window is initially optimal as the materials overlying the pial surface cause minimal scattering. Very large windows, i.e., $4 \times 6\,mm^2$, can be generated to facilitate easy positioning of electrodes and cannulae. However, a disadvantage of cranial windows in rats is the disruption of the intracranial pressure and exposure of the cortex to air. As a result, an inflammatory reaction is unavoidable even in the most carefully generated preparations. In our hands, rat cranial windows can be imaged for approximately 4 days, after which dural regrowth begins to degrade the imaging quality. Chronically implanted windows for repeated imaging in rats are rarely reported and the use of pharmacological agents to suppress inflammation may also affect the phenomenon under study, such as the magnitude of injury in experimental stroke models (Tuor *et al*, 1993). Window clarity may be maintained longer by overlaying the brain with inert substances such as Kwiksil silicone, as has been used in mice (Dombeck *et al*, 2009).

Cranial windows in mice are surgically less demanding, as the dura is thin and does not need to be removed for optical access. Detailed methods have been described for chronic bone-removed cranial windows (Holtmaat *et al*, 2009; Mostany and Portera-Cailliau, 2008) and semi-chronic thinned-skull windows (Yang *et al*, 2010). Here, we focus on a method where the skull is thinned, polished, and reinforced with a thin layer of glue and cover glass (Figure 3; Drew *et al*, 2010*b*). This method allows the generation of a stable and relatively large window, i.e., $2 \times 2\,mm^2$, which greatly minimizes disruption of the intracranial milieu, reduces inflammation, and prevents bone regrowth. Although the imaging depth and clarity are reduced compared with complete bone removal, polished and reinforced windows in mice provide excellent clarity for TPLSM imaging months after the initial surgery.

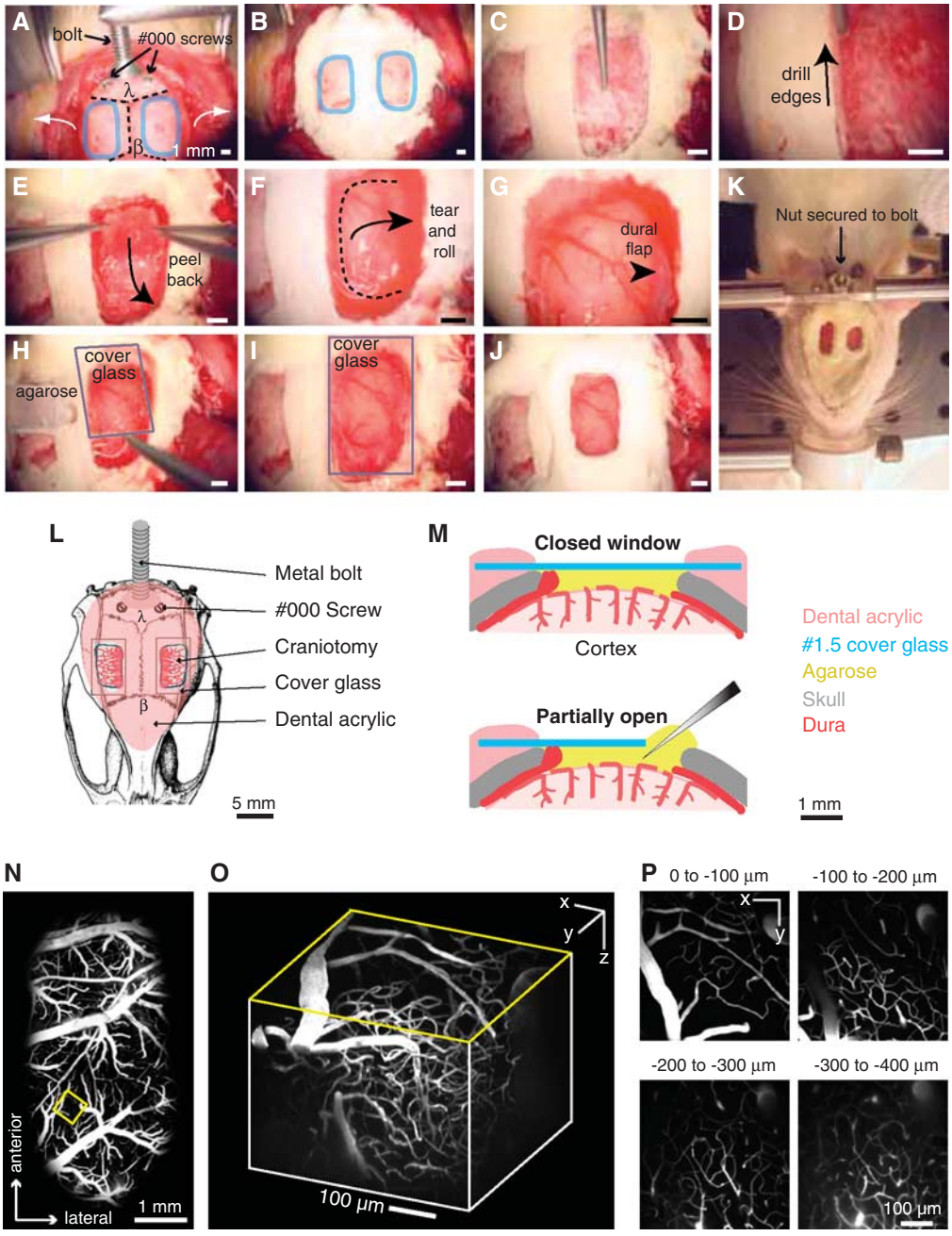

Figure 2 Procedure for rat dura-removed craniotomy. (**A**–**J**) Images of various stages in the procedure for generating an acute cranial window in rat. See text for detailed instructions. β = bregma and λ = lambda. (**K**) Bolt and nut system for securing the head during imaging of anesthetized preparations. (**L**) Schematic diagram showing dorsal view of the rat head mount and position of various pieces. (**M**) Schematic diagram showing cross-section of a rat cranial window. Lower panel shows modified window with opening that allows introduction of electrodes and injection pipettes. (**N**) Two-photon laser scanning microscopy maximal projection of vasculature visible throughout the entire cranial window after intravenous injection of fluoroscein-dextran dye. The image was generated by montaging several images collected with an $\times 4$ objective. A high-resolution image stack is collected from a region within the window (yellow square) using a $\times 40$ objective. (**O**) Three-dimensional rendering of the high-resolution image stack collected from panel **M**, generated by Voxx (http://www.nephrology.iupui.edu/imaging/voxx/). (**P**) Maximal projections over 50 μm of tissue taken at different depths below the pia. The image stack is the same as panel **O**.

Genetics and Behavior

Mice are becoming increasingly important with the advent of transgenic lines with fluorescently labeled components of the neurovasculature (Kleinfeld *et al*, 2011). Many are engineered to express fluorescent proteins under control of cell-specific promotors, which enable identification of almost any cell type, including glia (Nolte *et al*, 2001; Zhuo *et al*, 1997), excitatory neurons (Madisen *et al*, 2010), inhibitory

interneurons (Chattopadhyaya *et al*, 2004; Ma *et al*, 2006; Oliva *et al*, 2000; Tamamaki *et al*, 2003), pericytes (Zhu *et al*, 2008), arterial smooth muscle (Xin *et al*, 2002), endothelial cells (Motoike *et al*, 2000), and microglia (Jung *et al*, 2000). Some of these lines also express CRE-recombinase under the same promoters and can, in principle, be combined with animals or viruses carrying FLOXed gene cassettes to achieve cell-specific gene expression (Kuhlman and Huang, 2008; Madisen *et al*, 2010). This powerful strategy may be used to express sensors of cell activity (Akemann *et al*, 2010; Mank *et al*, 2008; Tian *et al*, 2009), light-based mediators of cell depolarization (Boyden *et al*, 2005) or hyperpolarization (Chow *et al*, 2010), chemical-based mediators of cell depolarization (Alexander *et al*, 2009; Fiacco *et al*, 2007), or small hairpin RNAs to disrupt specific signaling pathways (Babcock *et al*, 2005). In addition, a variety of mice with perturbations of potential vascular signaling pathways, such as nitric oxide synthase knockouts (Meng *et al*, 1996) or inositol-triphosphate 3 receptor knockouts (Li *et al*, 2005), are used in blood flow-related studies. In future studies, inducible knockouts will be of increasing value, as compensatory gene expression could be at play with chronic loss of gene function. Specific gene manipulations that lead to neurodegeneration (Kuchibhotla *et al*, 2009), white matter disease and spreading depression (Eikermann-Haerter *et al*, 2011), or vascular growth abnormalities (Murphy *et al*, 2008*a*) are potentially critical tools for studying vascular pathology in slowly progressing diseases, such as dementia and neurodegeneration (Misgeld and Kerschensteiner, 2006).

Transgenic technologies have not translated well to rats, which is unfortunate because the majority of our knowledge of rodent vascular physiology comes from rat studies. Rats also exhibit more complex behaviors and have classically been the model of choice for detailed fine motor control and sensory tasks (Hutson and Masterton, 1986; Knutsen *et al*, 2006; Krupa *et al*, 2001; Maaswinkel and Whishaw, 1999; Mehta *et al*, 2007) and memory-based tasks (D'Hooge and De Deyn, 2001) that may be relevant to vascular pathology. However, recent studies show that mice can be habituated and trained to perform head-fixed behavioral tasks (Komiyama *et al*, 2010; O'Connor *et al*, 2010). These techniques will be essential for linking blood flow and neural activity in awake preparations. Given the time investment required for behavioral training, the long-term stability of a mouse cranial window is an important benefit.

Detailed methods

Common surgical materials and procedures to prepare cranial imaging windows in rat and mouse are provided first. We then provide specific protocols for generating: (i) a dura-removed cranial window for studies in rat and (ii) a reinforced thinned-skull window for studies in mouse. All surgical procedures were approved by the Institutional Animal Care and Use Committees at UCSD and Cornell University.

Surgical Materials

The following materials are suggested when performing surgeries and TPLSM imaging of rodents.

Reagents

- Appropriate anesthetic (Table 1).
- Betadine (6906950; Butler Schein).
- Buprenorphine hydrochloride (Buprenex; 031919; Butler Schein, Dublin, OH, USA).
- Fluorescein-dextran or similar high-molecular-weight fluorophore (Table 2).
- Isopropyl alcohol, dissolved to 70% (v/v) in water (I9030; Sigma-Aldrich, St Louis, MO, USA).
- Lactated Ringer's solution (009846; Butler Schein).
- Modified artificial cerebral spinal fluid (mACSF), free of carbonate and phosphate (125 mmol/L NaCl, 10 mmol/L glucose, 10 mmol/L HEPES, 3.1 mmol/L $CaCl_2$, 1.3 mmol/L $MgCl_2$, pH 7.4; all chemicals from Sigma; Kleinfeld and Delaney, 1996). This recipe is used when forming a clear layer of agarose under the cover glass, as carbonate and phosphate precipitates are generated when regular ACSF is heated to melt the agarose. For simplicity, we use mACSF in both mouse and rat procedures, but regular ACSF may be used when agarose is not involved.
- Saline (009861; Butler Schein).
- Tool cleaning solutions (Surgical Milk, 014325 and Maxizyme, 035646; Butler Schein).

Disposables

- Bone wax (032005; Butler Schein).
- Cotton-tipped applicators (23-400-100; Fisher Scientific, Waltham, MA, USA).
- Cyanoacrylate glue (31428 H04308; ND Industries, Clawson, MI, USA).
- Dental cement (Grip Cement powder, 675571, and solvent, 675572; Dentsply, York, PA, USA).
- Drill burrs (For an air drill, 035624 and 035603; Butler Schein, for an electric drill, 19007-05; Fine Science Tools, Foster City, CA, USA).
- Kimwipes (06-666A; Fisher Scientific).
- Opthalmic ointment (039886; Butler Schein).
- Scalpel blades (12-460-448; Fisher Scientific).
- Screws, self-tapping #000 (FF000CE125; J.I. Morris Company, Southbridge, MA, USA).
- Surgical gauze (22-362-178; Fisher Scientific).
- Syringe needle (26 G, 036321; Butler Schein).
- Syringe plungers (1 cc, 9870250; Butler Schein).

Equipment

- Blood gas monitor (RapidLab 248; Bayer, or equivalent).

- Blood pressure monitor (BP1 and pressure transducer, World Precision Instruments (Sarasota, FL, USA) for intra-arterial; XBP1000, Kent Scientific (Torrington, CT, USA) for rat tail cuff measurements).
- Dental drill, air powered with foot-pedal control (Midwest Quiet Air; Dentsply). Electric powered drills are also suitable (K.1020; Foredom or EXL-M40; Osada, Los Angeles, CA, USA).

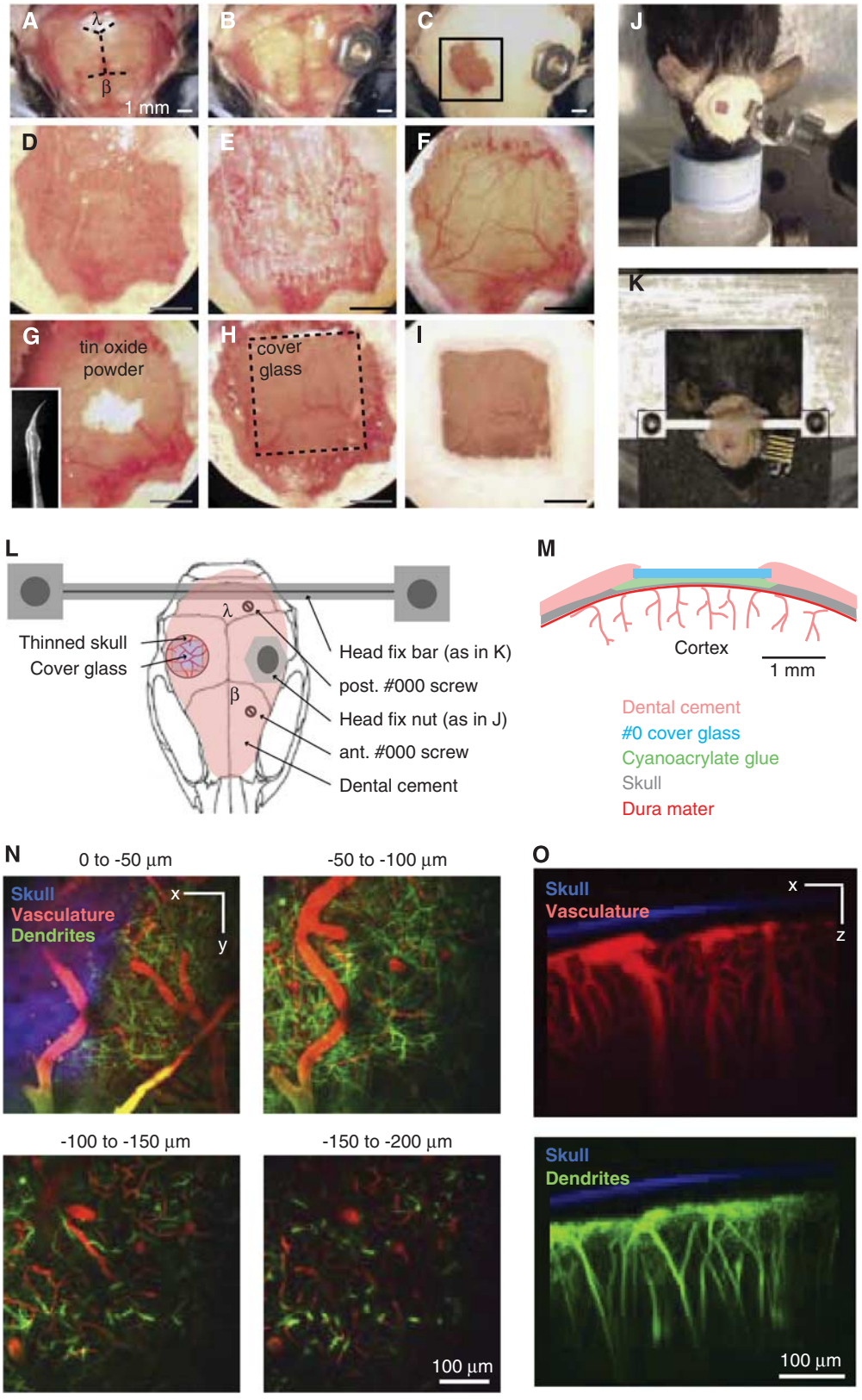

- Dissecting microscope (OPMI-1 FC or equivalent; Carl Zeiss, Thornwood, NY, USA).
- Electrical razor (Series 8900; Wahl, Sterling, IL, USA).
- Forceps, Dumont no. 55 (11255-20; Fine Science Tools).
- Forceps, serrated (11050-10; Fine Science Tools).
- Glass scribe to cut cover glass (08-675; Fisher Scientific).
- Heating pad with feedback regulation (Temperature control system, 40-90-8, rectal thermistor for rat and mouse, 40-90-5D-02, heat pad for rat, 40-90-2-05, heat pad for mouse, 40-90-2-07; FHC Inc., Bowdoin, ME, USA).
- Hemostats (no. 105-1105; George Tiemann, Hauppauge, NY, USA).
- Isoflurane vaporizer (IsoTec4; Datex-Ohmeda GE Healthcare, Waukesha, WI, USA).
- Pulse oximeter (MouseOx; Starr Life Sciences, Oakmont, PA, USA).
- Screwdriver, miniature (26B09.01; Garret Wade, Cincinnati, OH, USA).
- Stereotaxic frame, with rat or mouse ear and bite bars (Model 900; David Kopf, Tujunga, CA, USA).
- Surgical scissors, blunt end (14078-10; Fine Science Tools).
- Ultrasonic cleaner (15-335-30; Fisher Scientific).

Specific Materials for Rats

- Agarose, Type III-A (A9793; Sigma).
- Cover Glass, no. 1.5 thickness (12-541B; Fisher Scientific).
- Nut and bolt to secure the head (A35230-ND and H350-ND; Digi-Key, Thief River Falls, MN, USA) or a custom-made head frame (Kleinfeld *et al*, 2008).
- Periosteal elevator (RS-8820; Roboz, Gaithersburg, MD, USA).
- SurgiFoam (6547781; Butler Schein).
- Sutures, 4-0 silk (SS683; Covidien, Mansfield, MA).

Specific Materials for Mice

- Cover glass, no. 0 thickness (6661B40; Thomas Scientific, Swedesboro, NJ, USA).
- Insulin syringe, 0.3 mL volume with a 29.5-G needle (018384; Butler Schein).
- Nut and bolt to secure the head (H723-ND and R2-56X1/4-ND; Digikey) or a custom-made head-frame (Drew *et al*, 2010*b*).
- Silicone aquarium sealant (31001; Perfecto Manufacturing, Noblesville, IN, USA).
- Tin oxide powder (EQT-TINOX; Mama's Minerals, Albuquerque, NM, USA).

Surgical Preparation

Common Procedures: The following procedures are common across all laboratory animals.

- Ensure that your local Institutional Animal Care and Use Committee have approved all animal surgery procedures required for your experiment.
- Induce anesthesia (Table 1). Ensure a surgical plane of anesthesia by checking for a lack of the toe pinch reflex.
- Shave the scalp with an electrical razor.
- Secure animal in stereotaxic frame (Cetin *et al*, 2006).
- Apply opthalmic ointment to eyes to retain moisture.
- Inject lactated Ringer's solution intraperitoneally at a volume of 3 mL per kg every 2 hours to maintain body fluids and energy requirements.
- For sterile surgery, clean the scalp with betadine followed by 70% (v/v) isopropyl alchohol. After surgery, clean surgical tools by sonicating in Maxizyme and Surgical Milk in an ultrasonic cleaner. Dry the tools thoroughly and autoclave before each sterile surgery.

Optional Procedures

- Place a femoral vein catheter if drugs, such as the anesthetic α-chloralose (Table 1), are to be delivered intravenously. Similarly, a femoral artery catheter can be used to deliver drugs or monitor arterial blood pressure (see below; Waynforth and Flecknell, 1992). Of note, catheterization of the femoral vein distal to the tibial vein branch near the knee, may be suitable for survival studies as blood flow to the leg is not sufficiently impeded. However, survival following arterial catheterization is not advised.

Figure 3 Procedure for mouse polished and reinforced thinned-skull (PoRTS) window. (**A**–**I**) Images of various stages in the procedure for generating a chronic PoRTS window in mouse. See text for detailed instructions. β = bregma and λ = lambda. (**J**) Bolt and nut system for securing the head during imaging of anesthetized preparations. (**K**) Custom-machined crossbar head mount for awake preparations. The crossbar greatly reduces degrees of freedom for repeated imaging of the same location within the window. In this example, a connector was also implanted for repeated electrocorticogram recordings. (**L**) Schematic diagram showing dorsal view of the head mount and position of various components. The nut used in panel **J** is meant as alternative to the crossbar in panel **K**. Two #000 self-tapping screws can be added with the crossbar mount for added stability when imaging awake preparations. (**M**) Schematic diagram showing cross-section of a PoRTS window. (**N**) Maximal projections of a high-resolution image stack taken from a Thy1-YFP mouse (Zhang *et al*, 2005). Projections over 50 μm of tissue were made at different depths below the pia. The bone (blue) was detected by collecting second harmonic fluorescence at 450 nm with 900 nm excitation (Drew *et al*, 2010*b*). The vasculature (red) was labeled with intravenously injected Texas red-dextran (Table 2). The dendritic fields of neurons (green) are endogenous to the Thy1-YFP transgenic mouse line (Feng *et al*, 2000). (**O**) Maximal projection over a 250 μm of thickness of tissue in the coronal orientation showing the thinned skull in relation to the vasculature (top panel) and dendrites (bottom panel).

Table 1 Common anesthetic agents

Agent	*Route of delivery*	*Dose*		*Duration*	*Suitable for surgery?*	*Survival*	*Notes*	*Example (Reference)*
		Mouse	*Rat*					
Urethane	IP	750–1,000 μg/g	1,000 μg/g	6–8 hours	Yes	No	Make fresh for each day of surgery. Supplement 25% of induction dose as required. Sometimes combined with α-chloralose. Non-pharmaceutical grade anesthetics may need special approval by your institution.	Mouse (Dalkara *et al*, 1995) and rat (Kleinfeld *et al*, 1998)
α-Chloralose	IP (mouse); IV (rat)	50 μg/g induction; 50 μg/g supplement every 3 hours	55–65 μg/g induction; 40 μg/g/hour maintenance	8–10 hours	No	No	Does not produce surgical plane anesthesia. Transition to α-chloralose after surgery with isoflurane. Commonly used for functional hyperemia studies. Make fresh for each day of surgery. Non-pharmaceutical grade anesthetics may need special approval by your institution.	Mouse (Ayata *et al*, 2004) and rat (Devor *et al*, 2007)
Pentobarbital	IP	90 μg/g	40 μg/g	15–60 minutes	Yes	Yes	Narrow safety margin. Workup to adequate dose of anesthesia slowly. Supplement 10% of induction dose as required.	Mouse (Takano *et al*, 2006) and rat (Flecknell, 1987)
Ketamine mixed with xylazine	IP	60 μg/g (K) 10 μg/g (X) (mix in same syringe)	90 μg/g (K) 10 μg/g (X) (mix in same syringe)	20–30 minutes	Yes	Yes	Xylazine is co-injected as a muscle relaxant. Supplement only ketamine at 50% of induction dose as required. Ketamine is an NMDA receptor antagonist and may influence blood flow and stroke outcome.	Mouse (Takano *et al*, 2006) and rat (Flecknell, 1987)
Isoflurane	Inhalation	4% MAC for induction; 1–2% MAC for maintenance	4% MAC induction; 1–2% MAC maintenance	4–6 hours. Prolonged anesthesia leads to slow recovery	Yes	Yes	Useful for surgery because of easy titration and fast revival. Not optimal for functional hyperemia studies because of dampening of autoregulation and hyperemic response, especially when co-administered with nitrous oxide.	(Flecknell, 1987; Hoffman *et al*, 1991; Kim *et al*, 2010)

IP, intraperitoneal; IV, intravenous; MAC, mean alveolar concentration; NMDA, *N*-methyl-D-aspartate.

Table 2 Fluorescent agents for blood labeling

Target	*Dye or transgenic*	*Typical two-photon excitation (nm)*	*Emission peak (nm)*	*Notes*	*Source*	*Reference*
Serum	Fluorescein isothiocyantate-dextran (2 MDa)	800	530	Green emission	Sigma; FD2000S	Kleinfeld *et al* (1998)
	Texas red-dextran (70 kDa)	900	615	Red emission	Invitrogen; D-1830	Zhang *et al* (2005)
	Alexa 680-dextran (10 kDa)	1,280	680	Far red emission	Invitrogen; D34680	Kobat *et al* (2009)
RBCs	*Ex vivo* fluorescein labeling and IV injection	800	530	Labels cells rather than serum. Green emission.	Sigma; F6377	Hudetz *et al* (1995)

IV, intravenous.

- Intubate by means of a tracheotomy if the animal is to be artificially ventilated (Short, 1987). Alternatively, intubation can be performed noninvasively using a laryngoscope, which is suitable for survival experiments (Costa *et al*, 1986; Waynforth and Flecknell, 1992).

Physiological Monitoring

- Ensure heart and breathing rates are within a normal range using a pulse oximeter. These values should center around 6 and 1 Hz, respectively, for a rat and 10 and 2 Hz, respectively, for a mouse.
- Maintain body temperature at 37°C using a feedback regulated rectal probe and heat pad.
- Monitor arterial blood pressure continuously from a femoral arterial line. Alternatively, the tail cuff method can be used for rats to noninvasively measure blood pressure at intermittent time points. Mean arterial blood pressure should be maintained between 80 and 120 mm Hg.
- Arterial blood gas and pH can be measured once before and once after the experiment to ensure that values have not drifted over the course of the experiment. Blood pO_2 should be between 80 and 100 mm Hg, pCO_2 should be between 35 and 45 mm Hg, and pH should be between 7.35 and 7.45.

Acute Imaging Preparation for Rats: Dura-Removed Cranial Window: This preparation is primarily for imaging studies lasting 1 to 4 days and provides ample opportunity for the measurement and control of physiological parameters as well as for electrophysiological recording and drug delivery. It provides excellent optical clarity and exposes a large region of cortex, i.e., typically $3 \times 6\,mm^2$. Further, a maximal imaging depth of 500 μm is routinely achieved with 800 nm excitation when imaging blood vessels.

Mounting a head-frame:

1. Make a 4 to 5 cm incision down the midline of the scalp using a scalpel blade. Start the incision from between the eyes and cut to just caudal of the ears. Retract the scalp to the side of the head with four hemostats, two placed on either side caudally and two placed rostrally. Control bleeding with gauze.
2. Use a periosteal elevator to remove the thin periosteum from the surface of the skull (Figure 2A). Control bleeding from the areas of skin and soft tissue by applying constant pressure to the bleeding tissue with a pair of hemostats and removing excess blood with gauze and cotton applicators. Both the bregma (β) and lambda (λ) points should be visible on the exposed skull surface. If necessary, make additional cuts in the scalp to widen the field.
3. Stop any bleeding from vessels emanating from the skull by using light, focused abrasion with 1/2 mm dental drill burr.
4. Separate the temporal muscle from the temporal ridge, which runs along the lateral aspects of the skull (Figure 2A, white arrows). Apply direct pressure to the muscle where it attaches to the skull using the periosteal elevator. Avoid separating the muscle near the eye to prevent a rip to the infraorbital vein. Rather, separate the muscle as caudally as possible past the squamosal bone, which is roughly lateral to the lambda point. If desired, retract the muscle away from the skull with hemostats on both sides of the skull. Note that one can make bilateral windows to maximize use of each animal, and to potentially study bi-hemispheric changes in blood flow (Figures 2A and 2K).
5. Demarcate the location of the desired cranial window (Figure 2A, blue circles). As an example, primary somatosensory cortex, which is the part of parietal cortex, nominally lies between −1 and −5 mm relative to the bregma point and between 1 and 7 mm from the midline on the medial-lateral axis for rats (Paxinos and Watson, 1986). However, imaging of blood flow and/or cellular dynamics can be performed in any brain region that lies near the skull. The zygomatic arch may need to be removed when imaging more lateral structures such as auditory cortex.
6. Attach a metal connector to the skull with dental acrylic for immobilization of the head during imaging (Figures 2A and 2L). The connector could be a custom-fabricated metal frame (Driscoll *et al*, 2011*a*; Kleinfeld and Denk, 1999) or simply a nut and bolt system with a horizontal

cross bar, as shown (Figure 2K). Clean the contact regions of soft tissue to achieve a reliable connection between acrylic and bone. Apply a thin layer of cyanoacrylate glue to the bone. Introduce small self-tapping screws to the skull to reinforce the linkage of the connector to the skull, just posterior to lambda. Care should be taken when drilling pilot holes, as the transverse sinus lies directly beneath the lambda suture line.

7. Apply dental cement to the entire assembly. Cover the entire exposed skull surface with dental cement except where the window will be placed (Figures 2B and 2L). Fill the space between the skull and the retracted temporal muscle. Build a slight wall around the window region, which will eventually hold the agarose and keep the overlying cover glass from touching the brain surface. The wooden handle of the cotton-tipped applicator can be snapped to make a fine tip for trailing small amounts of dental cement around the window.

Dura-removed cranial window for rat:

8. Using a high-speed dental drill with a 1/2 mm burr, thin the skull evenly throughout the entire window (Figure 2C). Flush the surface frequently to reduce heating during drilling, and continue to thin until the underlying pial vasculature becomes visible after application of mACSF. The skull should be less than 1/4th of its original thickness at this point. This requires thinning through the vasculature of the skull, which may bleed, but can be controlled by flushing with mACSF.
9. Carefully thin the edges of the window with a 1/4 mm burr until a network of fine cracks in the bone begins to show (Figure 2D).
10. Soak the window with mACSF for 1 minute to allow the bone to soften, and then wick the liquid away with KimWipes.
11. Use a pair of forceps to gently separate connected segments of the bone flap from the skull, but do not yet remove the bone flap completely. Again, control bleeding from the dura by flushing with mACSF.
12. Soak the window with mACSF for another minute to soften the bone, and wick the liquid away.
13. Use forceps to grasp the far corners of the loosened bone flap, and slowly peel it away from the underlying dura mater (Figure 2E). Peel carefully at skull suture lines, as the underlying dura may be attached to the bone.
14. Flush the dural surface with mACSF and apply small pieces of SurgiFoam presoaked in mACSF to control bleeding. The serpentine-like dural vessels will be clearly visible at this point. All bleeding must be stopped before proceeding to the next step.
15. Retract the dura to the edges of the window (Figure 2F). This must be done with extreme care, because the dura is thin and close to surface of the cortex. First generate a small incision in the dura using the cutting edge of a 26-G syringe needle. Bend the needle to an obtuse angle with hemostats to ensure the cutting edge punctures the dural membrane but does not damage the underlying cortex.
16. Using two sharp no. 55 forceps, gently lift the dura away from the cortical surface, starting at the incision site, and tear in small increments (Figure 2F). Whenever possible, tear around large dural vessels to avoid bleeding. Limit any bleeding from dural vessels with small pieces of SurgiFoam soaked in mACSF or moistened KimWipes, twisted to a fine point with the fingers. If bleeding from the dura is excessive, flush with a slow flow of mACSF across the window until bleeding ceases.
17. Tear along three edges of the window, and roll the dural flap to the side of the window (Figures 2F and 2G). Flush the cortical surface with mACSF. It is crucial to avoid any damage to pial vessels. Hemorrhaging will alter cerebral blood flow, accelerate brain swelling, and severely degrade imaging quality. Removal of the dura and subsequent sealing of the window should be done swiftly, i.e., within 10 minutes, to avoid brain swelling.
18. Overlay the window with 1.5% (w/v) low-melting point agarose dissolved in mACSF (Figures 2H and 2M; Kleinfeld and Delaney, 1996). Dissolve the agarose in mACSF by heating in a microwave, using short periods of heating to prevent boiling. The agarose should be prepared ahead of time and maintained in a 60°C water bath. Draw the agarose mixture into a 1 mL syringe, and allow to cool slightly before applying 3 to 4 drops to the cortex; the agarose should not feel hot on the back of the hand. Then immediately seal the chamber using a precut cover glass that is larger than the size of the craniotomy. Ensure that the cover glass is not pressing against the cortical surface, as this will impede blood flow and lead to poor imaging quality over time (Figures 2I and 2M).
19. Apply dental cement to the edges of the cover glass (Figures 2J and 2M, upper panel). Build up the cement slightly to hold water for the dipping lens. Sealing the craniotomy is crucial to protect the cortex and suppress motion from cranial pressure fluctuations because of heartbeat and breathing. However, an edge of the window can remain uncovered to allow insertion of electrodes or micropipettes (Figure 2M, lower panel). In this case, apply ample agarose to the exposed edge as evaporation will eventually cause the agarose to dry. The perfusion of drugs over the cortical surface can also be achieved by adding tubing and an agarose-covered 'vent' that allows fluids to directly reach the cortical surface (Nishimura *et al*, 2010). Be aware that using

glass pipettes with diameters $>10\,\mu$m, such as those used to inject Ca^{2+} indicators, can cause cortical spreading depression and impair vascular reactivity for hours.

Preparing for imaging:

20. Suture the scalp so that it fits snugly around the head mount. Excess skin around the head mount should be cut early in the procedure, as bleeding from the skin takes 10 to 15 minutes to completely stop. Compress the cut edges with hemostats for 10 to 15 seconds to help minimize bleeding. When all bleeding has stopped, protect the exposed edges of the scalp by covering with dental cement. Apply additional dental cement around the metal connector for further reinforcement (Kleinfeld and Denk, 1999).
21. Stabilize the animal on an optical breadboard for imaging, using the frame as a head support (Figure 2K). The animal should be slightly suspended by the head mount, to prevent motion artifacts from breathing. Here, we use a custom-machined cross bar with a hole for the bolt. The bolt is inserted into the hole and a nut is then used to secure the animal's head in place. This preparation is stable for anesthetized preparations, but another bolt can be introduced to the anterior aspect of the skull for increased stability. Our animal restraint apparatus, constructed from optomechanical components, can be transported between surgical and imaging suites with the animal and all physiological monitoring devices assembled as one unit.
22. Before imaging, inject 0.3 mL of 5% (w/v) fluorescent-dextran dye dissolved in saline to label the blood serum (Table 2), either through the femoral artery/vein catheter or a tail vein. Extra fluorescein-dextran dye can be frozen in aliquots.
23. If the animal is meant to survive for more than 1 day, and is showing clear signs of pain when awakened, such as sustained immobility, decreased food and water consumption, and abnormal posture, e.g., hunched back, provide analgesia by injecting buprenorphine hydrochloride solution (10 to 50 μg per g weight of the animal) subcutaneously. Monitor animal periodically until it fully recovers from anesthesia.

Anticipated results for rat:

24. A window generated over the somatosensory cortex will reveal large proximal branches of the middle cerebral artery that can be several 100 μm in diameter. These large arteries traverse the entire window and eventually form anastamoses with arterioles branching from the anterior cerebral artery near the midline of the brain (Figure 2N; Blinder *et al*, 2010; Schaffer *et al*, 2006).
25. A web of smaller pial arterioles, typically $<100\,\mu$m in diameter, link these major branches and form redundant vascular loops over the cortical surface. In a $3\times6\,mm^2$ cranial window one might see ~100 penetrating arterioles that dive to feed subsurface microvessels (Blinder *et al*, 2010; Figure 2N).
26. Below the surface, penetrating arterioles begin to ramify into fine precapillary arterioles as shallow as 10 μm below the cortical surface, and continue to branch off over the depth of cortex (Tsai *et al*, 2009) (Figures 2O and 2P). Larger penetrating arterioles that feed deeper structures tend to branch less within the imaging depth accessible by TPLSM.
27. Capillary networks drain into penetrating venules and, like penetrating arterioles, run perpendicular to the cortical surface. Penetrating venules typically outnumber penetrating arterioles by a factor of $1.8\times$ in rat (Nguyen *et al*, 2011).
28. Penetrating venules drain into pial surface venules and, like arterioles form an intricate network on the surface. These venules either drain medially toward the superior sagittal sinus, or laterally toward the rhinal vein (Scremin, 1995). Venules can be differentiated from arterioles during imaging by a number of attributes, including: (i) a mottled appearance caused by slower moving RBCs; (ii) greater abundance of branches and cortical penetrations; (iii) a generally larger lumen diameter; (iv) a slower flow for the same lumen diameter; and (v) the direction of flow, as penetrating arterioles support flow into the brain while penetrating venules support outward flow. As arteriovenous anastomoses are not present in the normal brain, the individual arterial and venous networks can be traced without ambiguity once a vein or artery is identified.
29. For troubleshooting, refer to Table 3.

Chronic Imaging Preparation for Mice: Polished and Reinforced Thinned-Skull Window: This procedure allows repeated imaging for up to 3 months over a large cortical region, i.e., $2\times2\,mm^2$, without disrupting the intracranial milieu. Imaging depths of up to 250 μm are routinely achieved. It also permits the introduction of an electrode or micropipette to the brain through a separate drill hole.

Mounting a head frame:

1. Remove the scalp over the entire dorsal skull surface (Figure 3A). Use a scalpel blade to remove the thin periosteum from the surface of the skull.
2. Clean and dry the skull surface. Apply a thin layer of cyanoacrylate glue to the surface and allow the glue to dry thoroughly.
3. Attach a metal connector to the skull, away from the area of the desired window with a small dab of cyanoacrylate glue and allow the glue to dry thoroughly. Then secure the connector with a layer of dental cement. We adhere a small nut (no. 2-56) that can be later secured to the

Table 3 Troubleshooting for rat cranial window and imaging

Step	*Problem*	*Possible reasons*	*Solution*
1–3	Excessive bleeding from skin or skull	Inadequate depth of anesthesia. High blood pressure.	Increase the dose of anesthesia slightly. Control skull bleeding by allowing surface to dry and applying light abrasion to source of blood. Apply pressure to bleeding from skin and muscle by clamping with hemostats.
16	Excessive bleeding from dura	Torn dural vessel	Flush with mACSF in a syringe slowly and intermittently until bleeding stops. Apply moist SurgiFoam to the bleed, and wick away the moisture from the SurgiFoam with a KimWipe twisted to a fine point. In future, make a larger window so that dural vessels can be observed and avoided when removing the dura.
25	Poor imaging depth	Damage to pial vessels leading to subarachnoid hemorrhage. Incomplete removal of dura.	Discard this preparation. Avoid damage to pial vessels in the future.
	Movement artifacts	Improper sealing of the window. Air bubble in the agarose. Loose connector in head mount.	Ensure that the agarose concentration is correct and that an ample amount is added to the brain before overlaying with the cover glass. Tighten all connections in the head mount, and slightly raise the head from the body where the motion artifacts arise.
	Phototoxicity	Too much laser power	Ensure that the detector gain is set properly, and that all optics leading to the detectors are aligned. If blood vessels remain dim, not all the fluorescent dye was injected properly.

mACSF, modified artificial cerebral spinal fluid.

imaging setup using a bolt (Figures 3B, 3J and 3L). Seal the backside of the nut with tape to ensure that glue does not enter the threads.

4. Alternatively, attach a custom-made connector, in this case with two attachment points (Figures 3K and 3L). This greatly reduces the degrees of freedom and simplifies relocation of the same imaging field in longitudinal studies. A wide crossbar gives ample room for electrode placement and stimulation of vibrissae.
5. Cover the rest of the skull surface, excluding the location of the window, with a layer of dental cement (Figures 3C and 3L). Ensure that all exposed edges of the skin are covered by cement.
6. Stabilize the mouse in a head mount (Figures 3J and 3K). As with the restraint apparatus for rats describe above, a mouse apparatus can be made from commercially available miniature optomechanical components from Qioptiq (Rochester, NY, USA) or ThorLabs (Newton, NJ, USA).

Generating a polished and reinforced thinned-skull (PoRTS) window:

7. Thin a 2×2-mm^2 region over the somatosensory cortex with a 1/2-mm burr. Alternate between wetting the skull with mACSF and then drying the skull surface with a gentle stream of air; wet for cooling, and dry for thinning. The skull may bleed from the vessels in the inner cancellous layer, but can be controlled by flushing with mACSF (Figures 3D–3F). The skull begins to flex without breaking under the slight pressure of the drill when it is $\sim 50\,\mu$m thick, and the pial vessels should begin to be visible through the wet bone.
8. At this point, the bone must be thinned even further, and the speed and sharpness of the drill burr are critical. Change to a new drill burr and lightly shave the skull surface with small controlled movements while holding the drill like a pen. We find that a drill speed of $\sim$1,000 r.p.m. is appropriate at this stage. Small white spots within the bone, normally visible when moistened bone is $\sim 50\,\mu$m thick, will not be visible at the final skull thickness of approximately 10 to 15 μm (Figure 3F).
9. Polish the window region with tin oxide powder (Figure 3G). Attach a premade drill bit that has been dipped in silicone aquarium sealant and withdrawn, leaving a tapered whip (inset, Figure 3G). Place a small pinch of powder on the window along with a drop of mACSF. Agitate the slurry over the window for up to 10 minutes by gently touching the tip of the moving whip to the skull surface. Surface irregularities and adherent bone chips left by drilling in the previous steps should be removed after polishing. Flush away the tin oxide powder thoroughly from the window using mACSF and dry the bone thoroughly with a gentle stream of air.
10. Cut small square pieces of no. 0 cover glass, roughly 2×2 mm^2, by gently scoring separated horizontal and vertical lines in the cover glass with a scribe. Then place the cover glass in a Petri dish and shake vigorously to separate the glass pieces.
11. Apply a small dab of cyanoacrylate glue over the window using the wooden tip of a broken cotton-tipped applicator and quickly place an appropriately sized piece of no. 0 cover glass atop the glue (Figures 3H and 3M). Using forceps, push the glass so that it is in contact with the skull surface. Avoid creating bubbles underneath the cover glass. Allow the glue to

dry thoroughly for 10 minutes before proceeding. Excess cyanoacrylate glue can be removed from the upper surface of the cover glass with a scalpel after it is dried.

12. Seal the edges of the cover glass with dental cement and form a slightly raised well to hold water for the dipping lens (Figures 3I and 3M).
13. For some experiments, it may be desirable to inject dyes or insert electrodes into the tissue volume beneath the PoRTS window. A small hole can be added adjacent to the window, through which pipettes or electrodes can be introduced using a stereotaxic arm or Sutter manipulator (Stosiek *et al*, 2003). This hole can be resealed with bone wax after the experiment if the animal is to be imaged again in future sessions.

Preparing for imaging:

14. Stabilize the animal on an optical breadboard for imaging, using the frame as a head support. Our separate plate can be transported between surgical and imaging suites with the animal and all physiological monitoring devices assembled as one unit (Figures 3J and 3K).
15. Inject 0.05 mL of 5% (w/v) fluorescent-dextran dye dissolved in saline either through a femoral artery/vein catheter, tail vein, or infraorbital vein to label the blood serum (Table 2). For tail vein or infraorbital injections, use an ultrafine 0.3-mL insulin syringe with a 29.5-G needle.
16. If the animal is meant to survive for more than 1 day, and is showing clear signs of pain (see step 23 of last section), provide buprenorphine hydrochloride solution subcutaneously for analgesia.

Additional notes for awake imaging preparations:

17. More rigid head mounts are necessary for imaging awake animals. For increased stability, two self-tapping #000 screws can be added to the contralateral hemisphere of the skull before application of the dental cement, as shown in step 3 (Figure 3L).
18. Habituation to head fixation is important to reduced animal movement during imaging. A new animal can be gradually accustomed to head restraint over a period of 3 to 7 days, starting with 15 minutes sessions and working up to several hours (Drew *et al*, 2011). Before blood flow imaging, the mouse can be briefly anesthetized with isoflurane for an infraorbital injection of fluorescent-dextran dye. The dye will remain in circulation for several hours, and supplements can be given as necessary if the animal is re-anesthetized.

Anticipated results for mouse:

19. The cortical vasculature of the mouse is very similar to that of a rat, and can be thought of as a cropped, rather than scaled, version of the rat pial network (Blinder *et al*, 2010). In our example, we imaged a portion of the pial network after an intravenous injection of Texas red-dextran (Table 2), concurrent with yellow fluorescent protein (YFP)-labeled dendrites in the Thy1-YFP mouse line (Figures 3N and 3O) (Feng *et al*, 2000; Zhang *et al*, 2005). The average density of penetrating arterioles, and average surface area occupied by arterioles loops is very similar to the rat, but the total surface area of the mouse cortex is three times smaller (Blinder *et al*, 2010). As with rat, the subsurface microvasculature is highly tortuous and forms densely packed loops.
20. Detailed studies from mouse have revealed that neurons lie, on average, 15 μm away from the nearest microvessel, despite the fact that that cerebral vasculature only accounts for between 1% and 3% of the total cerebral volume (Tsai *et al*, 2009).
21. Two-photon imaging the vasculature through a PoRTS window requires transmission though the thinned bone and the dura, which attenuates the laser light and adds optical aberrations at greater depths (Drew *et al*, 2010*b*). However, despite this drawback, a well-prepared window will allow imaging of depths up to 250 μm below the pial surface for months (Figures 3N and 3O), and should show no sign of damage, such as angiogenesis and microglial reactivity.
22. In our hands, the success rate of the PoRTS window can be as high as 80%. In failed cases, the skull is breached or subarachnoid hemorrhaging occurs. These cases should be discarded.
23. The age of the mouse has a strong influence on the success of bone thinning. In adult mice 4 weeks or older, the rigidity of the more developed skull appears to prevent the bone from breaking, which is necessary to achieve the 10 to 15 μm optimal thickness. In younger mice, the soft skull is prone to break during the thinning process. Bleeding from the cancellous layer of the skull is also more prominent in older animals.
24. For troubleshooting, refer to Table 4.

Measurement of Blood Flow Dynamics in Single Cortical Vessels

In a typical preparation, we generate a cranial window over the hindlimb and forelimb regions of somatosensory cortex (Figure 4A). In the example given, we image cortical vessels through an acute rat window. Cortical regions that are responsive to stimulation can be mapped with intrinsic optical imaging, which reports a change in the ratio of oxy- to deoxyhemoglobin that occurs secondary to a change in neuronal activity (Frostig *et al*, 1990; Grinvald *et al*, 1986). The branching of pial arterioles

Table 4 Troubleshooting for mouse PoRTS window and imaging

Step	*Problem*	*Possible reason(s)*	*Solution(s)*
4	Head mount does not adhere to the skull surface.	Incomplete coating with cyanoacrylate glue before coverage with dental cement.	Ensure that the skull surface is dry before the application of a thin layer of cyanoacrylate glue to the entire skull surface. Allow the glue to dry thoroughly. A #000 self-tapping screw may be introduced to the skull, as describe for the rat cranial window above for added stability.
19	Poor imaging depth	Damage to pial vessels during thinning.	Discard this preparation.
		Skull in window is too thick or incompletely polished.	Avoid damage to pial vessels in future by thinning the skull more slowly and cooling with mACSF. Make the skull as thin as possible without causing damage.
	Movement artifacts	Loose connection to head mount	Tighten all connections in the head mount, and slightly raise the head from the body where the motion artifacts arise.
	Phototoxicity	Laser power is too high	See Table 3.

mACSF, modified artificial cerebral spinal fluid; PoRTS, polished and reinforced thinned skull.

and venules, which is unique to each animal, serves as useful fiducials to relocate the active region. The preparation is then moved to the TPSLM imaging setup, and the vasculature is labeled with an intravenous bolus of fluorescein-conjugated dextran. The cerebral vasculature within the window is first mapped at low resolution with a $\times 5$ objective (Figure 4A). High-resolution imaging of surface pial vessels, penetrating vessels, and subsurface capillaries can then be performed in smaller regions with a high numerical aperture water dipping objective, such as the LUMPLFL $\times 40$ 0.8 numerical aperture objective from Olympus (Center Valley, PA, USA) (Figure 4B).

User-Defined Scan Patterns to Simultaneously Measure Red Blood Cell Velocity and Lumen Diameter: When the serum is labeled, RBCs exclude the high-molecular-weight dextran dye and appear as dark shadows moving against a bright fluorescent background. This differential staining is the basis for measuring RBC velocity using laser scanning microscopy (Kleinfeld *et al*, 1998; Villringer *et al*, 1989). We used custom software to direct the imaging laser beam in a user-defined path within the imaging plane (Figure 4B; Driscoll *et al*, 2011*a*; Valmianski *et al*, 2010), following earlier work (Göbel and Helmchen, 2007; Göbel *et al*, 2007; Lillis *et al*, 2008). Linear segments of constant scan speed traverse along the length of the center of the vessel and across the width of the vessel to measure RBC speed and lumen diameter, respectively. These linear scan segments are connected by polynomial splines, where connecting portions of the scan are accelerated to allow for rapid data collection across multiple vessels (Figure 4C; Driscoll *et al*, 2011*a*).

The resulting line scan is a space–time image, typically displayed with the individual scan lines stacked on top of each other (Figure 4D). In principle, many vessels can be measured simultaneously. However, greater distances traversed by the laser will reduce the sampling frequency of RBC velocity, and a 1 to 2 kHz line scan rate is typically required for accurate sampling of the movement of RBCs in pial arterioles (Driscoll *et al*, 2011*a*). Further, the RBC speed in penetrating vessels is only measurable when a part of the vessel is parallel to the imaging plane.

Calculating Red Blood Cell Velocity: Portions of the scan path along the centerline of the vessel lumen reveal angled streaks within the cascade image (right panel in Figure 4E). Moving RBCs in flowing vessels sampled at a sufficient rate will appear as diagonal streaks. A stationary or stalled flow will result in vertical streaks. In the limiting case of extremely fast flowing vessels, the streaks will become horizontal, and velocity data cannot be extracted (see also Table 5 for troubleshooting). The centerline velocity is proportional to the slope of the RBC streaks, measured from vertical. Determining this slope is most efficiently performed with a Radon transform of windowed portions of the data (Drew *et al*, 2010*a*), which is available in the MATLAB Image Processing Toolbox (Mathworks, Natick, MA, USA). The direction of flow can be extracted from the sign of the slope and the direction of the line scan sweep.

A velocity time series is calculated by taking successive time windowed portions of the line scans. The size of the window must be sufficiently short to resolve the highest velocity modulation frequency, the heart rate, which is ~ 6 Hz for rats and ~ 10 Hz for mice. In addition, the window size must be large enough to capture enough streak lines so that the Radon transform has sufficient data to calculate an accurate velocity value, but small enough to prevent smoothing out the higher frequencies of the velocity data. We find that a window size of 40 ms is a good compromise, which yields a Nyquist frequency of 12.5 Hz. We further use a window spacing of 10 milliseconds.

In addition to heart rate, other physiological signals detected in the RBC velocity of anesthetized rat include breathing at ~ 1 Hz and vasomotion at ~ 0.1 Hz (Kleinfeld and Mitra, 2011; Mayhew *et al*, 1996), whereas an awake mouse will have vasomotion ranging from 0.1 to 1 Hz (Drew *et al*, 2010*b*); breathing is often not detectable in the awake state (Figure 5; Drew *et al*, 2011).

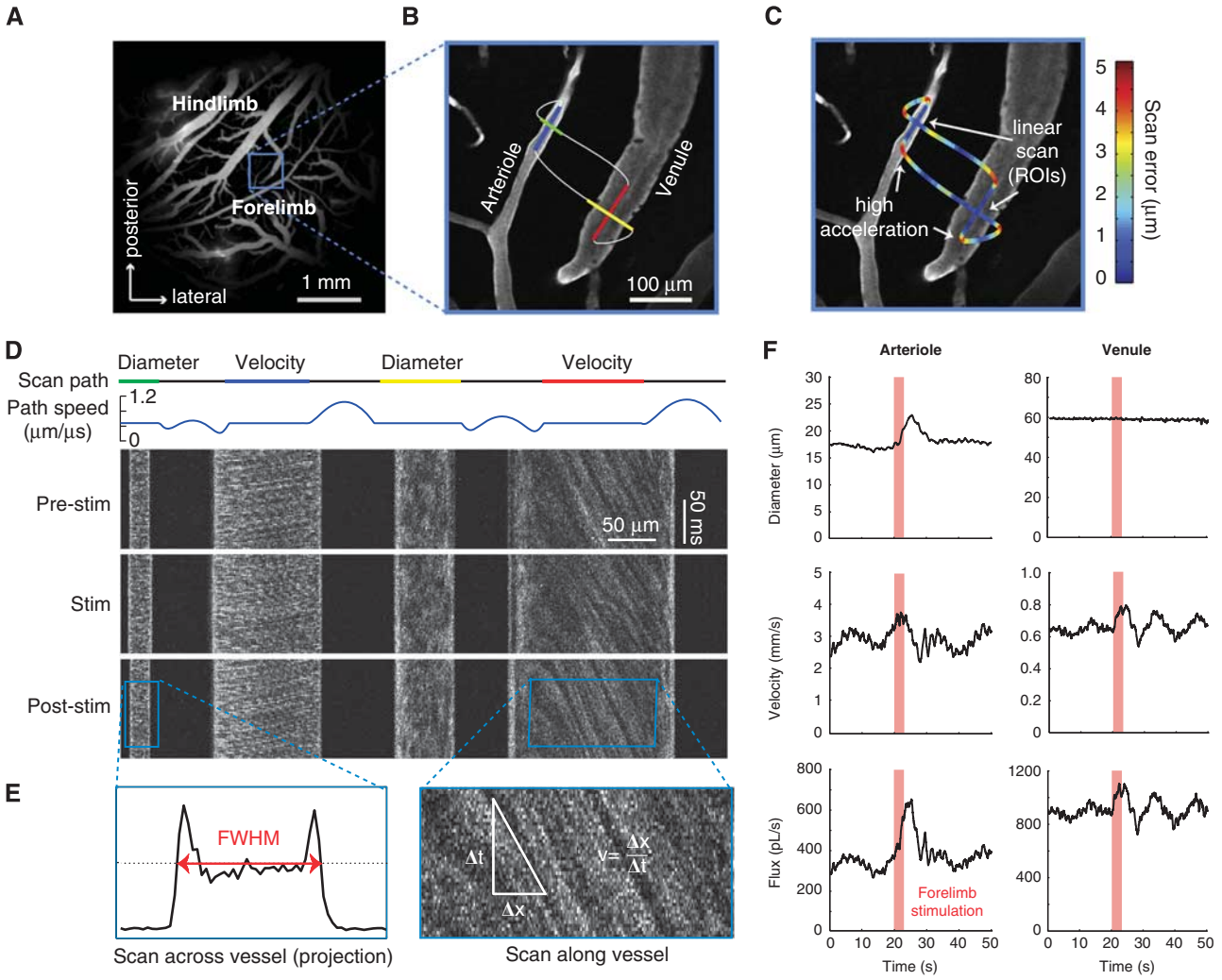

Figure 4 Simultaneous measurement of lumen diameter and red blood cell velocity in multiple vessels using spatially optimized line scans. (**A**) Image of fluorescein-dextran-labeled vessels in the rat somatosensory cortex taken with a $\times 4$ objective. The forelimb and hindlimb regions were mapped by intrinsic optical imaging (Frostig *et al*, 1990). (**B**) High-magnification image of a surface arteriole and venule in the forelimb region collected with a $\times 40$ objective. The pattern of the two-photon scanning laser is superimposed. Portions of the scan path along the length of the vessel are used to calculate red blood cell (RBC) velocity, whereas portions moving across the width of the vessels are used to calculate lumen diameter (Driscoll *et al*, 2011*a*). Scans were acquired at a rate of 733 scan cycles per second. (**C**) The scan path is colored to show the error between the desired scan path and the actual path the mirrors traversed. The error along linear portions of the image is typically $< 1\ \mu$m and increases when the mirrors undergo rapid acceleration. The error between successive scans of the same path is $< 0.15\ \mu$m, several times lower than the point-spread function of a two-photon laser scanning microscopy. (**D**) The upper traces show the scan path and mirror speed as a function of time. Note that portions used to acquire diameter and velocity data are constant speed. The line scans generated from the path can be stacked sequentially as a space–time plot as shown in the lower image panels. Each image panel shows ~ 100 milliseconds of data collected before, during, and after an electrical stimulation of the contralateral forelimb of the anesthetized rat. The stimulus was a 1 mA current, delivered for 3 seconds at 3 Hz with a 100-milliseconds pulse width (Devor *et al*, 2007). (**E**) Vessel diameter is calculated as the full-width at half-maximum of a time-average of several scans across the width of a vessel (left). Red blood cell velocity is calculated from the angle of the RBC streaks (right; Drew *et al*, 2010*a*). (**F**) Data traces of lumen diameter, RBC velocity, and RBC flux for the arteriole and venule after processing to remove heartbeat and smoothing with a running window. Figure adapted from Driscoll *et al* (2011*a*).

Even when anesthetized, the imaged vessel may move slightly with tissue swelling caused by heart beat, breathing, stimulated increases in blood flow, or edema in stroke models. In practice, most of the movement is within the axial plane. As a quality control measure, velocity line scans can be tested on capillaries, which are only 3 to 5 μm in diameter. A small shift in the axial plane will lead to a loss of the RBC streaks. Under the proper conditions, one should be able to hold the capillary scan without losing streaks for tens of minutes. Similarly, on the brain surface, an arteriole can be scanned simultaneously with a neighboring venule, which should exhibit little or no change in lumen diameter.

Table 5 Troubleshooting for blood flow measurement

Problem	*Possible reason*	*Solution*
RBC velocity line scan generates horizontal lines	RBC velocity is too fast	Use a faster scan speed, and increase acceleration of mirrors between linear stretches of the scan pattern. Zoom out on larger vessels, or use a lower magnification lens, i.e. $\times 20$, to observe each RBC over a longer distance. Scan along a longer length of the vessel lumen. Choose a smaller diameter vessel. There is a limitation to the speed that can be measured in surface pial vessels. Pial venules and subsurface vessels are generally all slow enough to be measured.
Line scan streaks are not straight	Vascular segment to be measured is not completely within the imaging plane	Ensure that a sufficient length of the line scan traverses the centerline of the vascular lumen

RBC, red blood cell.

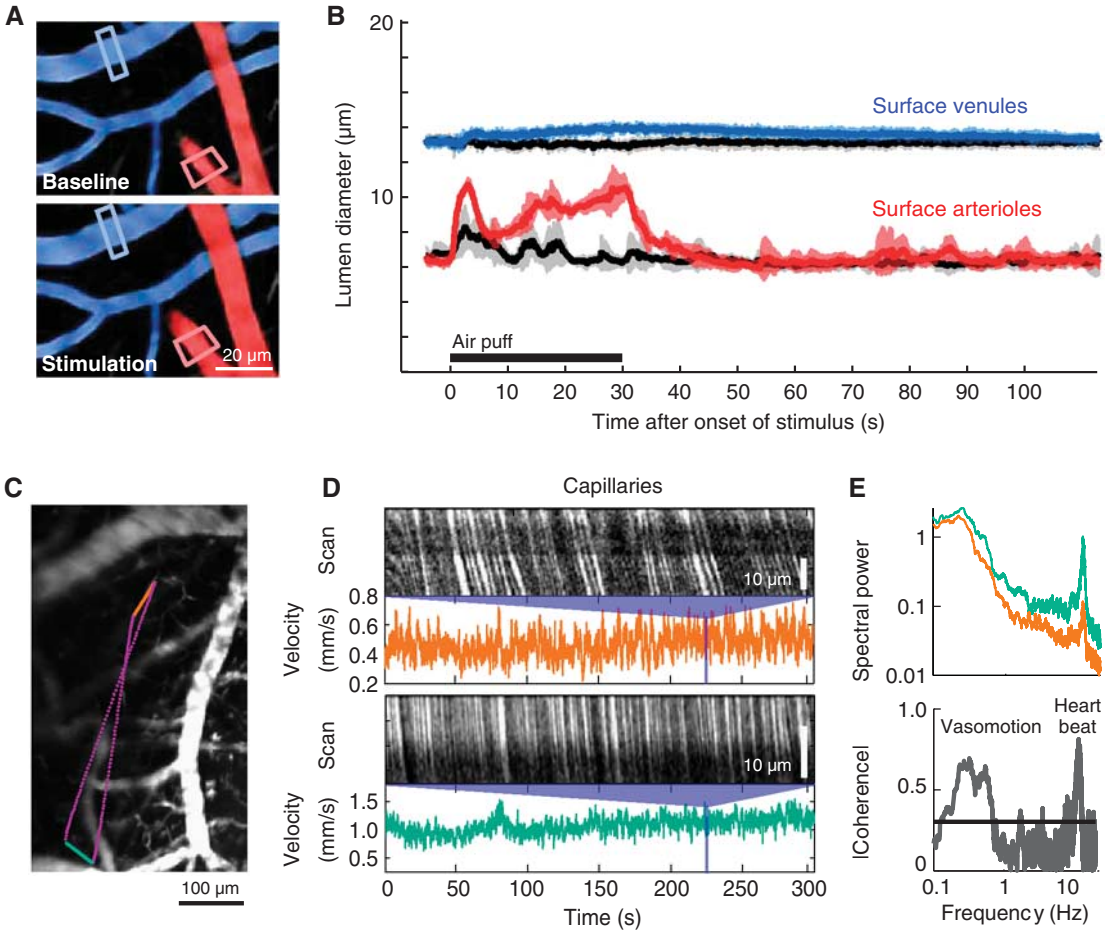

Figure 5 Evoked dilation and basal rhythms of cortical vessels in awake mouse. (**A** and **B**) Arterioles show rapid and sustained dilation in response to prolonged contralateral whisker stimulation. In contrast, venules respond with limited and delayed dilation. The stimulus was an 8 Hz, 30 seconds train of air puffs to the contralateral whisker pad (black bar). Images in panel **A** are maximal projection of fluorescein-dextran-labeled vasculature over 90 μm of tissue taken 51 days after implantation of a polished and reinforced thinned-skull window and pseudocolored to show arterioles (red) and venules (blue). (**C**) Red blood cell velocity measurements from distant capillaries in an awake mouse. Colored lines show the laser-scan path: green and orange are constant velocity segments along capillaries and purple segments are minimum time segments between capillaries. (**D**) Space–time plots of line scan data for each of the two capillaries with the calculated instantaneous red blood cell (RBC) velocity for over 300 seconds of data. (**E**) Power spectra for the two RBC velocity traces in panel **D** (0.083 Hz bandwidth; top) and magnitude of the spectral coherence between the velocities of the two capillaries as a function of frequency (0.1 Hz bandwidth; bottom). Horizontal black line denotes a significance level of $P = 0.05$. Vasomotion and heartbeat are significantly coherent at $P < 0.01$. Figure adapted from Drew *et al* (2011).

Maximum Measurable Red Blood Cell Velocity: For relatively fast blood flow, the pattern of fluorescence will change too much to between successive line scans to allow for accurate reconstructions of the flow velocity. As a naive estimate of maximum measurable blood flow velocity, if the RBC diameter is $\sim 5\,\mu$m, and successive cells are spaced $5\,\mu$m apart, then the pattern of light and dark will have a spatial period of $\sim 10\,\mu$m. In this case, the cells cannot move more than $5\,\mu$m between successive scans without the image aliasing. At a scan rate of 1 kHz across $100\,\mu$m, the maximum flow rate that can be measured is ~ 25 mm/s. However, in actual blood flow data there are typically lower spatial frequency modes, which exist because of unequal spacing of RBCs, different RBC widths because of cell orientation, and location in the focal plane etc. Because of this, the width of the dominant streaks in the scan lines is typically larger than the $10\,\mu$m naive estimation, and thus maximum measureable flow velocity can be higher than the calculation above (Schaffer *et al*, 2006; Shih *et al*, 2009). Measuring high-velocity vessels requires taking data across a longer portion of vessel, to ensure that there is a sufficient amount of information to reconstruct the streak lines, and that only a fraction of the labeled plasma moves out of the field of view in each successive scan (Table 5).

Calculating Lumen Diameter: As with the velocity calculation, the diameter calculation is taken from a time windowed portion of the data. The same window size and spacing used for velocity is typically used for diameter so that both parameters can be calculated on the same time scale. Vessel diameter is calculated as full-width at half-maximum of the vessel profile for each window (left panel in Figure 4E). Note the intensity profile tends to increase near the edges because of the exclusion of RBCs from the glycocalyx, which generates two peaks. The two outermost half-maximum points of these peaks are used to calculate the vessel boundary. Linear interpolation is used to add subpixel accuracy to the diameter measurement.

Estimating the Flux of Red Blood Cells: There are two limiting cases for the flux. When the diameter of the vessel allows the passage of RBCs only in single file, as for the case of capillaries, the flux of RBCs is just the number of RBCs that pass per second (Chuquet *et al*, 2007; Kleinfeld *et al*, 1998). In this limit, the blood plasma has an essentially constant velocity profile as a function of distance from the center of the vessel, then the velocity falls rapidly to zero near the walls. The thin layer of plasma near the walls acts as a lubricating layer that, together with the glycocalyx, minimizes friction (Secomb *et al*, 1998).

When the diameter of the vessel is much greater than that of the RBC, the flow is laminar and nearly parabolic as RBCs flow in parallel streams (Rovainen *et al*, 1993; Schaffer *et al*, 2006). The two vascular parameters, RBC velocity and lumen diameter, are combined to calculate the volume flux, i.e., RBCs and plasma, for each vessel. Flux is a more complete description of blood flow in single vessels, as RBC speed and lumen diameter can change independently of each other (Kontos, 1989; Shih *et al*, 2009). The volume flux through the vessel is given by

$$\vec{F} = \langle \vec{v} \rangle A = \frac{\pi}{8} \vec{v}(0) d^2$$

where $(\vec{v})$ is the average RBC velocity over A, the cross-sectional area of the vessel lumen, $\vec{v}(0)$ is the time-averaged RBC velocity at the center line of the vessel, and d is the lumen diameter. Note that this formula underestimates the flux as the nonzero spatial extent of the RBC flattens the parabola of Poiseuille flow. Empirical corrections have been discussed (Nishimura *et al*, 2010) and a first-order correction, i.e., for $a \ll d$ where a is the effective diameter of the RBC, is given by replacing the term $\vec{v}(0)$ of the above equation with

$$\vec{v}(0)[1 - (4/3)(a/d)^2].$$

As an example, we measure the change in flux at the level of single penetrating vessels in response to somatosensory stimulation. A line scan frequency of 733 Hz was used to capture the lumen diameter and RBC velocity of an arteriole and a venule nearly simultaneously. Both diameter and RBC velocity in the arteriole respond to stimulation (left column in Figure 4F). The flux through the arteriole increases to a peak of 86% over baseline, compared with a much smaller peak increase of 29% and 24% for diameter and velocity measurements alone, respectively. The increase in RBC velocity is partially masked by a peak in the underlying vasomotor fluctuation, but remains a significant increase over an average 1-minute period of basal activity.

In contrast to the arteriole, a neighboring venule exhibits no change in lumen diameter, but a 23% change in RBC velocity. As a result, the flux increases in the venule by 23% as well (right column in Figure 4F). This increase in venular flux would not be detected with methods that measure diameter only. This caveat should also be kept in mind with arterioles, as functionally evoked diameter changes may not occur along the entire length of the vascular tree. Changes in RBC velocity, however, will be detectable both upstream and downstream of the point of resistance change.

Similarly, the underlying vasomotor oscillation exists only in the RBC velocity traces for each vessel, likely because changes in resistance are occurring upstream of the measured vessel segments. Vasomotion is also commonly observed as slow changes in arteriole diameter (Lefer *et al*, 1990; Ngai *et al*, 1995). Here the amplitude of the vasomotion oscillations in the venular RBC velocity trace increases after stimulation, consistent with previous findings (Figure 4F; Vetri *et al*, 2007).

Example applications

Imaging Stimulated and Basal Hemodynamics in Awake Mice

Cortical vascular dynamics are profoundly different in the awake vs. anesthetized states (Martin *et al*, 2006). Anesthetics are known to reduce the functional hyperemia response (Lindauer *et al*, 1993) and also slow vasomotor oscillations (Drew *et al*, 2011). Here, we show the quantification of blood flow both at and below the cortical surface in awake mice (Figure 5). Mice were habituated to head fixation and blood flow was measured in single vessels through a chronically implanted PoRTS window. Robust arteriole dilations could be evoked by prolonged contralateral whisker stimulation (Figures 5A and 5B, red). Pial venules, typically thought to be static in terms of diameter, show a delayed and weak dilation in the awake state (Figures 5A and 5B, blue). Both arteriolar and venular responses were strongly suppressed by the use of urethane, a common anesthetic (Drew *et al*, 2011). These data suggest that functional hyperemia changes detected by BOLD fMRI may be dominated by large changes in arteriole volume, in agreement with recent studies (Kim and Kim, 2011), rather than in venules as predicted by the 'balloon' model (Buxton *et al*, 1998).

Dilatory events are relatively slow and diameter measurements can be analyzed from full-frame movies collected at six or more frames per second, in addition to line scans. Measurement of RBC velocity in subsurface capillaries always requires rapid line scanning to accurately quantify (Figures 5C and 5D). We create a user-defined scan path across two capillaries separated by a 500 μm distance to examine the coherence of blood flow between distant regions in the same cortical hemisphere (Drew *et al*, 2010*b*). Spectral analysis of the RBC velocity data reveals expected frequency peaks at $\sim$10 Hz for heartbeat (Figure 5E), and a slow vasomotor oscillation at 0.1 Hz (Mayhew *et al*, 1996). Vasomotion occurs on a relatively global level within cortex, as opposed to the more spatially restricted blood flow changes that are coupled with local cortical activity, discussed in the next example. The source and function of the vasomotion remain to be determined. It may originate from intrinsic $[Ca^{2+}]_{int}$ oscillations in arteriole smooth muscle, synchronized activity of cells in cortex, or from subcortical nuclei that project onto cortical cells or vasculature (Drew *et al*, 2008).

Simultaneous Imaging of Blood Flow and Local Cellular Activity During Neurovascular Coupling in Anesthetized Rat

An important goal is to identify the cell types and signaling pathways that regulate neurovascular coupling. The activity of various neuronal cell types and astrocytes can be monitored in superficial cortex by bulk loading the tissue with functional dyes, in this case Oregon green bapta-1-AM, to detect changes in $[Ca^{2+}]_{int}$ (Garaschuk *et al*, 2006; Stosiek *et al*, 2003; Figure 6A). The Ca^{2+} indicators may be injected by micropipette into the active region through a vent in the cranial window under two-photon guidance (Figure 2M) or before sealing the window during the initial craniotomy procedure.

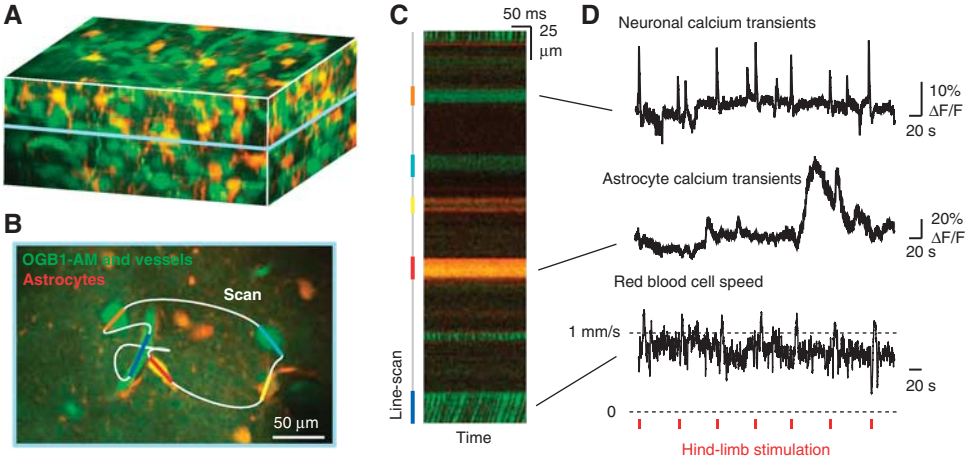

Figure 6 User-defined scan pathways to simultaneously record blood flow and activity from neighboring cells. (**A**) Neurons and astrocytes are labeled with the Ca^{2+} reporter OGB1-AM (Oregon green bapta-1-AM; green). Astrocytes can be distinguished from neurons using the astrocyte-specific label SR101 (red; Nimmerjahn *et al*, 2004). Blood plasma is stained with fluorescein-dextran (green; Table 2) and vessels are distinguished from cells based on their irregular and elongated morphology (Valmianski *et al*, 2010). (**B**) The user-defined scan path records cellular $[Ca^{2+}]_{int}$ signals and blood cell movement. Constant velocity regions of the line scan used for data collection are shown in color and the accelerated portions that connect the linear segments are show in white. (**C**) A space–time plot generated from the line scan collected in panel **B**. The corresponding regions of the scan path are shown on the left of the image. (**D**) Traces of functional changes in $[Ca^{2+}]_{int}$ and blood flow; note flow changes concurrent with electrical stimulation of the contralateral hindlimb. Figure adapted from Kleinfeld *et al* (2011).

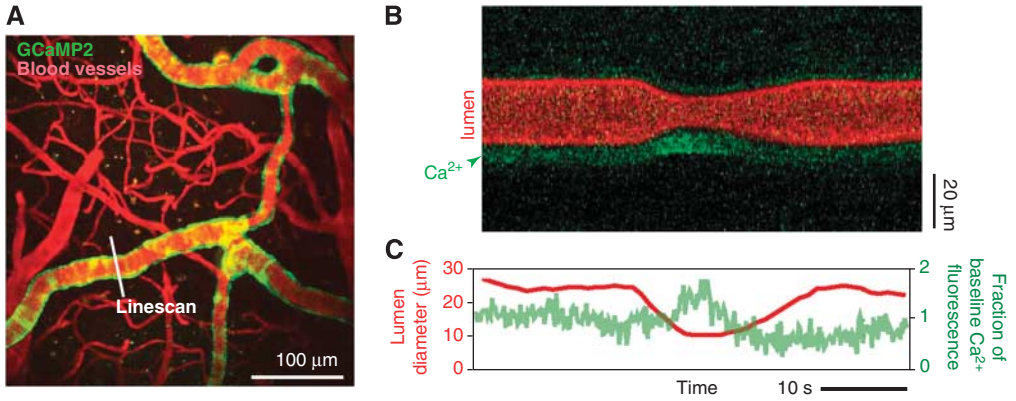

Figure 7 Measurement of arteriole smooth muscle activity concomitant with vasodynamics. (**A**) Maximal projection of image stack from an α-actin-BAC-GCaMP2 mouse, which expresses the genetically encoded Ca^{2+} indicator GCaMP2 in smooth muscle (Ji *et al*, 2004). GCaMP2 (green) is visible in concentric rings of smooth muscle surrounding the vascular lumen labeled with Texas red-dextran (red; Table 2). (**B**) A space–time plot resulting from a line scan taken across the lumen of a pial arteriole. (**C**) An increase in GCaMP2 fluorescence is seen concomitant with a vasoconstriction. The change in vessel diameter seen in this example is a vasomotor event. In these transgenic animals, the observable changes in $[Ca^{2+}]_{int}$ concentration are limited to large contractile events; thus the present data must be considered as preliminary. Figure adapted from Kleinfeld *et al* (2011).

User-defined line scans are used to measure the activity of neurons and astrocytes concurrent with blood flow in a neighboring microvessel through the cranial window of an α-chloralose anesthetized rat (Figure 6B). Astrocytes are selectively labeled by the rhodamine derivative SR101 in the same tissue to distinguish them from neurons in a second imaging channel (Nimmerjahn *et al*, 2004). The resulting line scan image contains stereotypical angled streaks for calculation of RBC speed, as well as intensity traces from selected neurons and astrocytes, similar to that seen in Figure 4 (Figure 6C). Fast $[Ca^{2+}]_{int}$ transients are indicative of action potentials (Figure 6D; Kerr *et al*, 2005). Calcium transients coincide with periods of hindlimb stimulation, but also occur independently. The astrocytic $[Ca^{2+}]_{int}$ transient shows slower kinetics, typically lasting several seconds. In this case, the astrocytic response does not appear to lock to hindlimb stimulation. Concurrently collected blood flow data show increases in microvessel RBC speed that tightly track periods of stimulation. Although we have measured a single microvessel and a few cells in this example, it is possible to guide the laser scan path with a cell identification algorithm to measure from up to a 100 cells within the same imaging plane at 100 Hz (Valmianski *et al*, 2010). Further, capillary flow speeds may be slow enough to collect line scans from up to 10 capillaries simultaneously in a small region of cortex.

The approach described here allows one to correlate the specific location and activity of defined cell types with local changes in blood flow. Transgenic mice with different neuronal subtypes labeled with fluorescent proteins may aid the separation of responses from different cell populations (Sohya *et al*, 2007). Finally, genetically encoded $[Ca^{2+}]_{int}$ sensors exclusively expressed in a specific cell type can be essential in separating signals from individual cells, which may be an issue with bulk loading of all cellular compartments (Shigetomi *et al*, 2010; Tian *et al*, 2009).

Measurement of Arteriolar Smooth Muscle Function

Techniques to measure activity in arterial smooth muscle are critical for understanding the vasoactive signals that lead to functional hyperemia. The combined action of vasoactive transmitters released from all local cells, astrocytic or neuronal in origin, eventually translate into a contraction or relaxation of arteriole smooth muscle. Elevation of cytosolic $[Ca^{2+}]_{int}$ is the major determinant of smooth muscle contractility (Karaki *et al*, 1997).

The observation of smooth muscle $[Ca^{2+}]_{int}$ dynamics *in vivo* has been impeded as a result of the difficultly in selective loading of Ca^{2+} dyes into the vasculature. However, transgenic animals with endogenous expression of genetically-encoded Ca^{2+} sensors, for instance GCaMP2 through GCaMP5, hold great promise for imaging studies on neurovascular coupling (Ji *et al*, 2004). Here, the cortical vasculature was imaged through a PoRTS window (Figure 7A). GCaMP2-labeled smooth muscle cells ensheath the arteriole network, but not the venular network, as expected. Line scan measurements reveal strong spontaneous constrictive events in the arterioles correlated with increases in smooth muscle $[Ca^{2+}]_{int}$ (Figures 7B and 7C). Although the animals described here appear to have a limited range of responsivity, making $[Ca^{2+}]_{int}$ transients associated with smaller diameter changes difficult to resolve, improved sensors such as GCaMP3, may report $[Ca^{2+}]_{int}$ changes over a wider dynamic range of arteriole reactivity (Tian *et al*, 2009). Such animals could

potentially allow direct visualization of the neurovascular coupling process, i.e., the direct action of neuronal or astrocytic activity on local smooth muscle activity.

Imaging of Blood Flow in Deep Cortical Layers

An important development in TPLSM is the ability to image deep cortical layers that are responsible for the output of neuronal processing (Helmchen and Denk, 2005). Penetrating arterioles are separated from the tissue by the fluid-filled Virchow-Robin space. As the penetrating arteriole plunges deep into cortex, the vascular adventitia fuses with the glial limitans, forming a close association between the cortical parenchyma and the vasculature. It is at this close point of interaction that neurovascular coupling is likely to initiate (Hamel, 2006).

Longer wavelengths of light penetrate deeper into tissue as a result of reduced scattering, absorption, and optical aberration. In this example, excitation with 1,280 nm wavelength light from a Ti:sapphire-pumped optical parametric oscillator enabled TPLSM imaging through the entire depth of mouse cortex, i.e., over 1 mm deep, through a dura-intact cranial window (Figure 8A; Holtmaat *et al*, 2009; Kobat *et al*, 2009). Red blood cell velocities in capillaries could be resolved as deep as 900 μm into cortex (Figures 8B and 8C). The red-shifted dye Alexa 680-dextran was used to label the blood serum. This dye emits at a longer wavelength than the usual fluorescein, and the emission is less strongly absorbed by blood and tissue on the way to the detector. To take full advantage of deep tissue imaging, red-shifted functional dyes, such as Ca^{2+} and voltage sensors that can be two-photon excited at longer imaging wavelengths, would need to be developed. This would complement the ability to visualize vascular dynamics concurrent with cellular activity in deeper cortical layers.

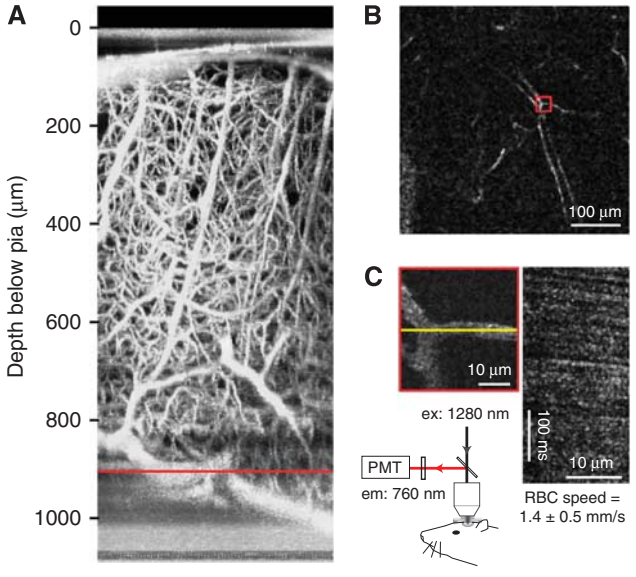

Figure 8 Deep imaging of cortical angioarchitecture and blood flow. (**A**) Maximum intensity projections of mouse cortical vasculature in the coronal orientation. The image stack was collected over the entire depth of cortex through a dura-intact cranial window. To reduce scattering and improve imaging depth, a long wavelength excitation (1,280 nm) was used and the blood plasma was labeled by intravenous injection of Alexa 680-dextran (Table 2). (**B**) Single planar image taken from panel **A** at the depth of the red line. (**C**) Magnified image and line scan taken from a vessel from the region in the red box in panel **B**. Adapted with permission from Kobat *et al* (2009).

Measuring Partial Pressure of O_2 in Blood Vessels and Tissue

A critical determinant of neuronal metabolic activity is the availability of O_2 supplied through the blood. Further, a feedback mechanism may exist, as ambient pO_2 levels also influence the dilatory capacity of cerebral arterioles (Gordon *et al*, 2008). The mechanisms that govern pO_2 in brain tissue are not well understood. In recent work, a small molecule pO_2 probe, Ptp-C343, was developed and imaged with an optimized TPLSM setup (Finikova *et al*, 2008; Sakadzić *et al*, 2010). Subsequent to two-photon excitation, the probe decays by phosphorescence—a process that is accelerated when the O_2 tension is high. The partial pressure of oxygen, pO_2, can then be calculated offline by fitting the phosphorescence decay to an established calibration curve.

The probe enables measurement of absolute pO_2 concentration either within the vascular lumen following intravenous injection or the cortical parenchyma following intracerebral injection. The example of Figure 9 shows how pO_2 can be measured at the level of single vessels through a dura-intact cranial window in mouse, after intravenous delivery of the probe. The vascular architecture was first determined by conventional imaging with fluorescein-dextran (Figure 9A). The Ptp-C343 phosphorescence originating from the lumen of a single penetrating arteriole and penetrating venule was then sampled at $\sim$150 μm below the cortical surface (Figure 9B). As expected, the penetrating arteriole exhibited shorter phosphorescence lifetime, consistent with a higher pO_2, compared with an adjacent penetrating venule with lower pO_2 (Figure 9C). Importantly, intravascular pO_2 could be measured over various depths of cortex (Figures 9D and 9E).

Combined with the TPLSM blood flow measurement techniques, we have described (Figure 4) small molecule O_2 probes will aid the study of O_2 transfer from vasculature to tissue during functional hyperemia during health and various disease states (Girouard and Iadecola, 2006). Indeed, Lecoq *et al* (2011) has elegantly demonstrated the feasibility of measuring cerebral blood flux, neuronal activity, and pO_2 simultaneously in olfactory bulb (Figures 9F and 9G). Recent work by Devor *et al*, (2011) has extended similar measurements to the superficial layers of cortex.

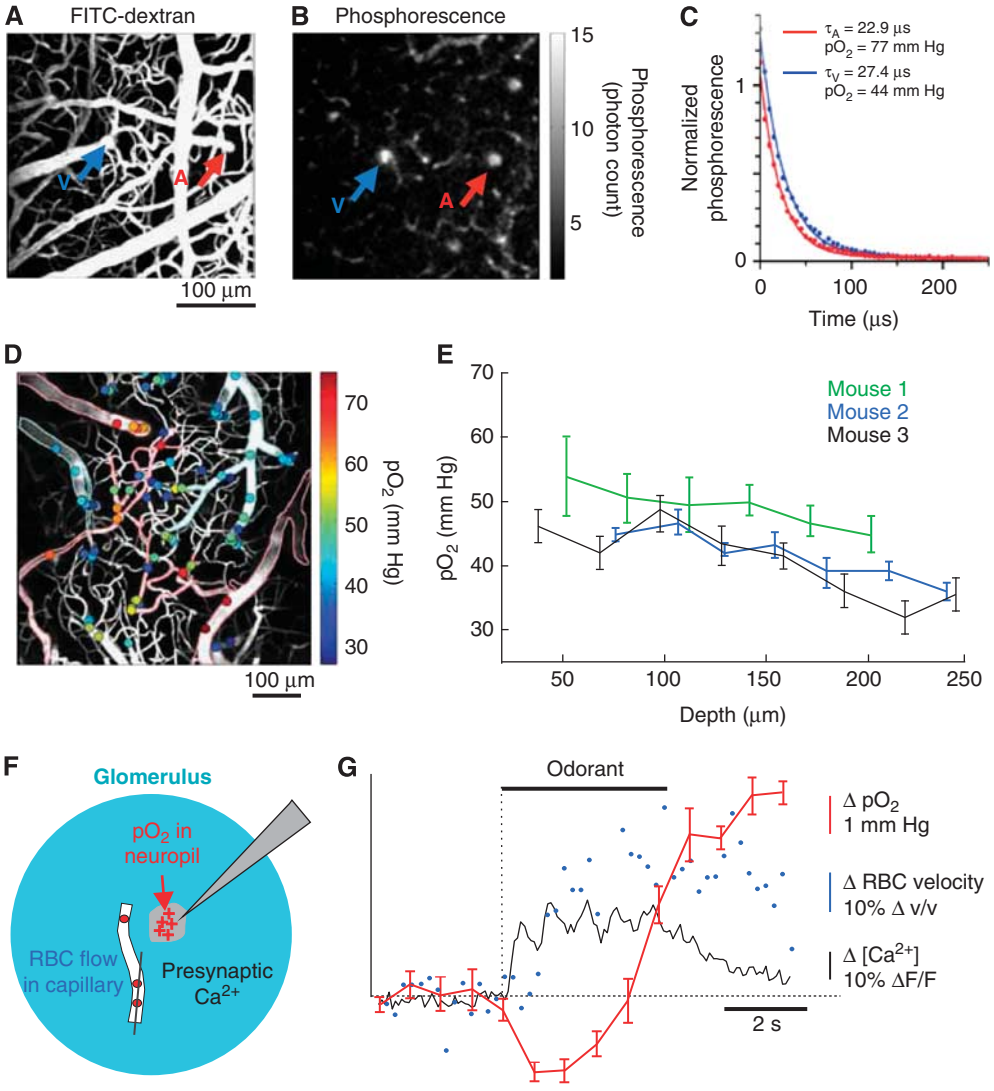

Figure 9 Imaging of intravascular partial pressure of oxygen. The mouse cerebral vasculature was imaged through a dura-intact cranial window following intravenous delivery of the phosphorescent O_2 probe PtP-C343. (**A**) Maximum intensity projection of the vascular architecture along *z* direction of a 250-μm-thick image stack. The vasculature was labeled with fluorescein-dextran and the location of a penetrating arteriole and a penetrating venule are marked with red and blue arrows, respectively. (**B**) PtP-C343 phosphorescence intensity image of penetrating vessels obtained at 166 μm depth below the cortical surface. The intensity bar shows the average number of phosphorescent photon counts in each pixel collected during phosphorescence decay. (**C**) Experimental measurement and corresponding single-exponential fits of a phosphorescence decay from the penetrating arteriole and the penetrating venule. (**D**) Measured pO_2 values in microvasculature at various depths (circles), overlaid on a maximal intensity image of the vascular structure (gray, arterioles are outlined in red). The color bar shows the calculated partial pressure of oxygen at the measured location. (**E**) The intravascular pO_2 plotted as a function of cortical depth in three mice averaged across all vessels excluding pial arterioles. Adapted with permission from Sakadzić *et al* (2010). (**F** and **G**) Schematic of experiment and superposition of presynaptic Ca^{2+}, red blood cell (RBC) velocity, and pO_2 responses in a single glomerulus during odor stimulation. Error bars indicate standard error of the mean. Adapted with permission from Lecoq *et al* (2011).

Manipulating Blood Flow with Photothrombosis and Laser Ablation of Single Vessels

The majority of current preclinical stroke models focus on large-scale ischemic strokes that manifest severe behavioral deficits (Ginsberg and Busto, 1989). However, small cortical infarcts are prominent in cases of human small vessel disease and dementia, and are clinically difficult to detect (Kövari *et al*, 2007; Suter *et al*, 2002). Optical access to the vasculature offers the opportunity for laser-mediated formation of intravascular clots in single vessels, as a model to study the effects of small-scale stroke in rats and mice (Hua and Walz, 2006; Mohajerani *et al*, 2011; Nishimura *et al*, 2006, 2007). On the cortical surface, single vessel thrombosis is achieved by irradiating the lumen of the target vessel with a focused green laser to activate the circulating photo-

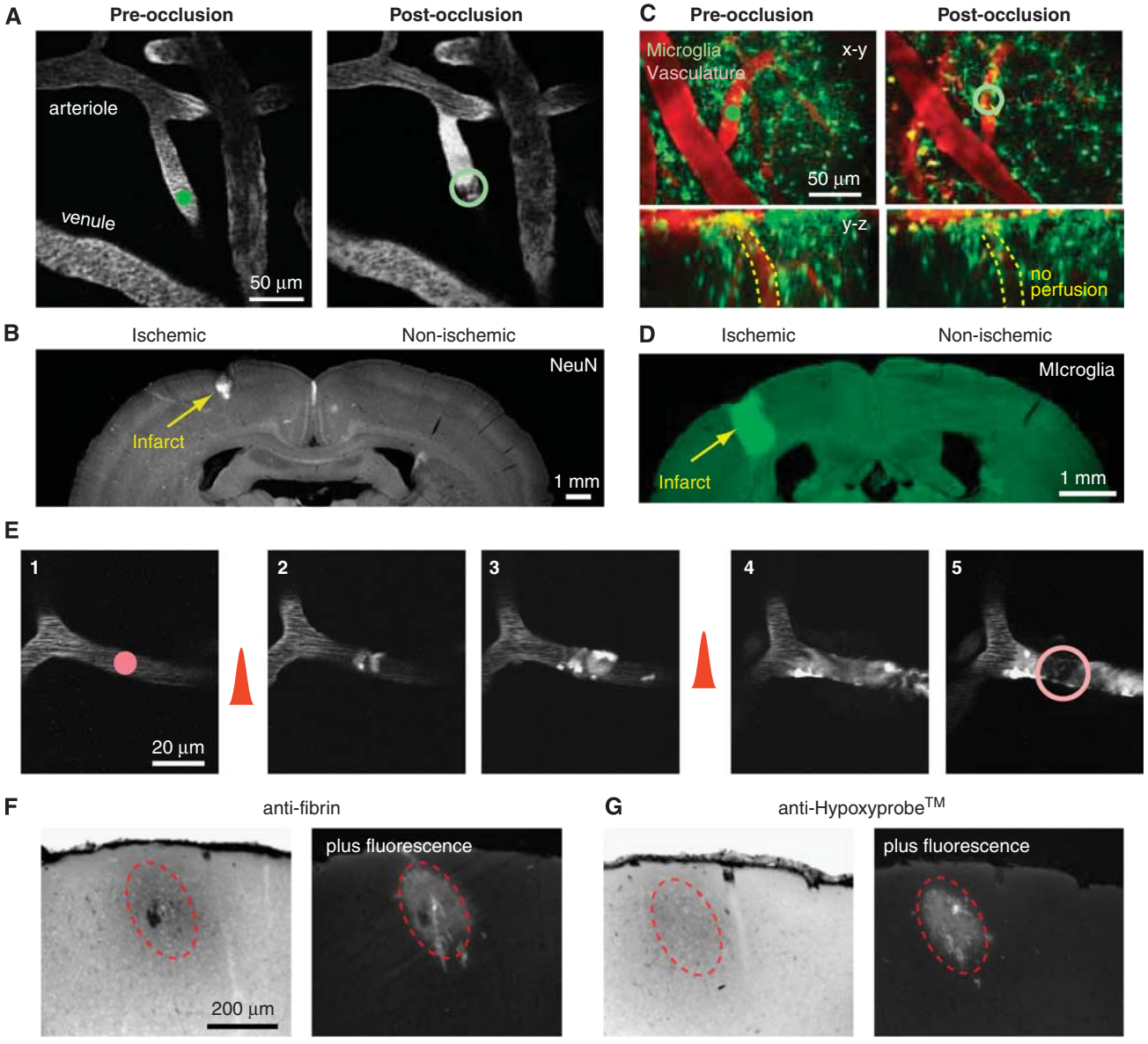

Figure 10 Manipulation of blood flow in single-cortical vessels using auxiliary lasers. (**A**) Rose Bengal-mediated photothrombosis of a single penetrating arteriole on the pial surface. Occlusion was achieved after 1 minute of irradiation with a green laser focused in the lumen of the target vessel (filled green circle in left panel). The thrombus formed by irradiation sits stably within the lumen surrounded by stagnant serum (open green circle in right panel). (**B**) Tissue infarction 7 days after penetrating vessel occlusion, as assessed by NeuN immunohistology. (**C**) Photothrombosis of a single mouse penetrating arteriole through a PoRTS window. The CX(3)CR1 mouse line expresses GFP in microglia and monocytes (Davalos *et al*, 2005). (**D**) A dense column of activated microglia is visible in the cortex 7 days following single vessel occlusion. (**E**) Targeted clot formation in a deep microvessel using amplified ultrashort laser pulses. Occlusion was achieved after repeated sub-threshold pulses of irradiation with an amplified 800 nm laser focused in the lumen of the target vessel (filled red circle in left panel). The thrombus formed by irradiation sits stably within the lumen (open red circle in right panel). (**F** and **G**) Immunohistochemical detection of a fibrin-containing clot and an associated, highly localized region of tissue hypoxia following occlusion of a single microvessel. The dotted circles in panels **F** and **G** demarcate the location of tissue pathology. Adapted from Blinder *et al* (2010), Drew *et al* (2010*b*), and Nishimura *et al* (2006).

sensitizing dye, Rose Bengal (Schaffer *et al*, 2006; Watson *et al*, 1985). Below the cortical surface, thrombosis is achieved by focusing high-fluence, 100 to 300-fs pulses of near infrared light into the vessel lumen (Nishimura *et al*, 2006). Nonlinear absorption ensures that the laser injury is limited only to the plane of focus. In both cases, damage of the vessel wall induces clot formation in the lumen.

In the first example, we use Rose Bengal irradiation to occlude one of many penetrating arterioles visible on the pial surface through a dura-removed cranial window in rat (Figure 10A) or a PoRTS window in a CX(3)CR1 transgenic mouse with green

fluorescent protein (GFP)-labeled microglia (Figure 10C). Measurements of blood flow can be made before and after the occlusion, to confirm successful occlusion and to examine adaptive flow changes in neighboring vessels (Nishimura *et al*, 2010; Schaffer *et al*, 2006). One week after occlusion, a localized cortical infarct can be identified by immunostaining for the pan-neuronal marker NeuN (Figure 10B) or by aggregation of immune cells in the infarcted tissue (Figure 10D), consistent with the concept that penetrating arterioles form bottlenecks within the cortical vasculature (Blinder *et al*, 2010; Nishimura *et al*, 2007).

In the second example, we consider a microvessel that is 10 μm in diameter and 250 μm below the cortical surface (Figure 10E). Uniform flow is seen in the vessel before irradiation, as evidenced by streaks in the full-frame image (panel 1 in Figure 10E). After the first burst of pulses with the high-fluence laser, the vessel wall is compromised and fluorescein-dextran becomes trapped in the endothelium (panels 2 and 3 in Figure 10E; Chen *et al*, 2009). A second burst of pulses leads to cessation of flow and a stagnant pool of fluorescent plasma downstream of the clot (panels 4 and 5 in Figure 10E). The clot can be located *post hoc* in tissue slices using fibrin immunohistochemistry (Figure 10F). Further, the spatial extent of tissue ischemia associated with the clot can assessed with Hypoxyprobe, a histological marker of tissue hypoxia, but not tissue death (Figure 10G; Nishimura *et al*, 2006).

Finally, longitudinal *in situ* tracking of transgenic mice with TPLSM can be key method for assessing neuronal structure following all sizes of stroke. By using Thy1-YFP mice, the fine dendritic structure of deep neuronal populations can be imaged over a period of hours to days following stroke (Brown *et al*, 2007; Mostany and Portera-Cailliau, 2011; Zhang *et al*, 2005). In the example of Figure 11, blood vessels (red channel in Figure 11A) as well as the dendritic arbors of layer 5 neurons (green channel in Figure 11A) are imaged through a dura-intact cranial window; note that dendrites can similarly be imaged through a PoRTS window (Drew *et al*, 2010*b*). Injection of Rose Bengal and irradiation of the vasculature with a broadly focused green laser causes flow to cease in all pial vessels in a region roughly 1 mm^2 in area (right panel in Figures 11A and 11B). In this case, severe ischemia leads to rapid dendritic damage over a period of 30 minutes, as evidenced by blebbing of the dendritic shafts (Figures 11C and 11D). In contrast, regions bordering the core, i.e., the penumbra, typically exhibit mild ischemia and reversible dendritic damage (Zhang and Murphy, 2007). Surprisingly, microbleeds about 100 μm in diameter, caused by ablation of small cortical vessels, do not lead to overt dendritic damage (Rosidi *et al*, 2011). The signaling pathways that govern this dendritic plasticity (Dancause *et al*, 2005; Winship and Murphy, 2008), may have therapeutic implications for large and small-scale strokes.

Summary and future steps

Two-photon microscopy provides a number of advantages that will aid the study of the mechanisms

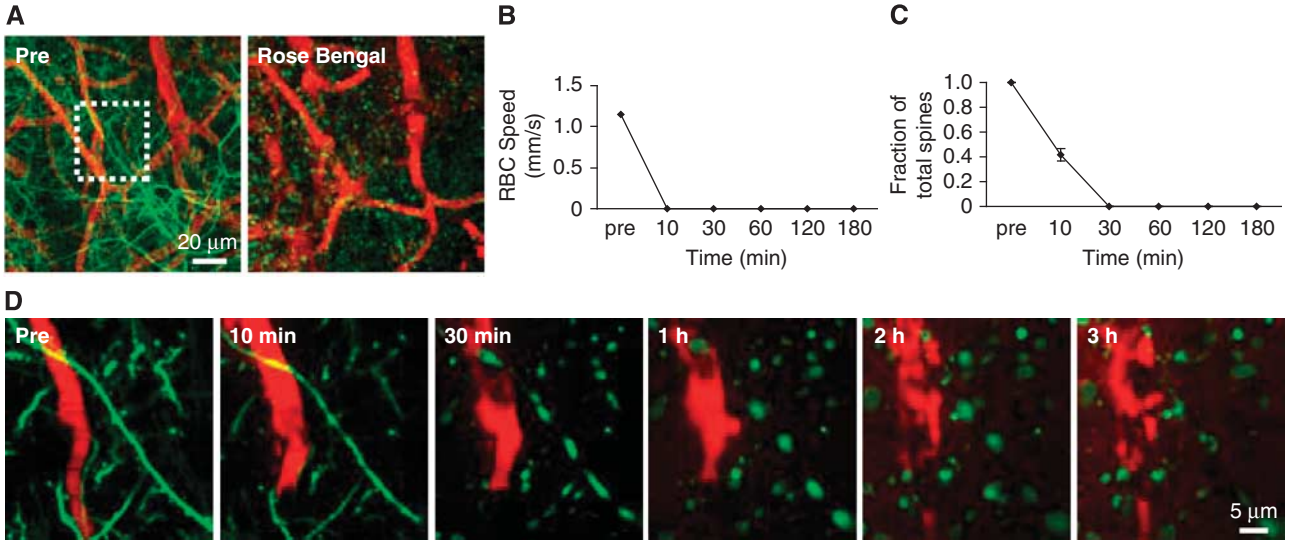

Figure 11 Imaging of neuronal structure following targeted stroke. (**A**) Images from a Thy1-YFP mouse showing Texas red-dextran-labeled vasculature (red) and neuronal dendrites (green). The images are maximal intensity projections of the first 100 μm of the cortex before and 30 minutes after photoactivation of circulating Rose Bengal. (**B** and **C**) Quantification of red blood cell (RBC) velocity and dendritic spine number for the animal shown in panel **A**. (**D**) Dendritic structure was completely lost within 30 minutes of photothrombosis. Residual blood flow after stroke was zero and reperfusion did not occur. Apparent clotting and breakdown of capillaries were seen 30 minutes after photothrombosis. Adapted with permission from Zhang *et al* (2005).

underlying neurovascular coupling and cerebrovascular disease in animal models, including: (i) the resolution needed to visualize single cortical vessels and their surrounding cells; (ii) penetration depths of 250 μm through a PoRTS window and 500 μm with dura-removed craniotomies at 800 nm excitation, and even deeper imaging with longer excitation wavelengths; (iii) reduced photodamage and photobleaching; (iv) high-speed user-defined line scans for near-simultaneous measurement of RBC velocity, lumen diameter, and local cellular activity; (v) longitudinal imaging the same preparation over several months; and (vi) the ability to image vascular dynamics deep in the cortex of awake mice.

A wide variety of functional fluorescent dyes that currently exist can be exploited for studies of neurovascular control. Recent focus has been on Ca^{2+} sensors to study cellular activity. Organic-based sensors such as OGB1-AM have the advantages of labeling both neurons and astrocytes, along with a meshwork of processes that intervene between cell bodies. However, the cellular source of a signal may be difficult to resolve when focusing on fine processes. Genetically encoded Ca^{2+} sensors that are expressed only in specific target cell populations will resolve any ambiguities of signal source. Cyclic adenosine monophosphate sensors would also be of value considering that Ca^{2+}-independent pathways may also be involved in neurovascular control.

Similarly, the intermixing of cell types within a small tissue volume also hinders electrophysiological and pharmacological approaches to query the role of cell types in neurovascular coupling. New advances with light activated opsins (Lee *et al*, 2010) or engineered receptors with unnatural affinities for exogenous chemicals (Alexander *et al*, 2009; Fiacco *et al*, 2007) may help to unravel issues with cellular specificity (Kleinfeld *et al*, 2011). However, caveats should also be considered, as activation of one cell type does not preclude activation of nontargeted cells linked within the same circuitry. To test for specificity of action, opsins could be used in conjunction with bolus-loaded Ca^{2+} sensors (Figure 6) that report the activity of surrounding cells. Another approach would be to inhibit critical signaling pathways. The manipulation of cell-specific vasoactive signaling cascades will be an important step in dissecting the chemical basis of neurovascular coupling, but will also be the most challenging as new tools to knockdown gene expression will need to be developed (Kleinfeld *et al*, 2011).

There is also an additional need for tools to quantify volume conduction of vasoactive transmitters concurrent with measurement of blood flow. We recently described the use of CNiFERS, HEK293 cells that co-express the genetically encoded Ca^{2+} sensor TN-XXL with a muscarinic acetylcholine receptor. Following implantation directly into cortex, CNiFERS enable real-time measurement of extracellular acetylcholine concentration (Nguyen *et al*, 2010). Further, injectable protein-based detectors of neurotransmitter concentration, such as the EOS glutamate sensor, may be useful for studying vasoactive signaling (Okubo *et al*, 2010).

Future imaging studies related to neurovascular control are likely to make exclusive use of awake, behaving mice to circumvent problems associated with anesthesia, such as suppressed autoregulation (Drew *et al*, 2011). Genetically encoded indicators of physiological function as well as methods to optically stimulate cellular activity and specific signaling pathways are well suited for studies in awake, behaving mice (Airan *et al*, 2009; Drew *et al*, 2010*b*; Zhang *et al*, 2007).

We have described methods that can be used to observe and manipulate the fine-scale of neurovascular coupling, i.e., at the interface between cells and vasculature. However, it is important to realize that the somatosensory-evoked hemodynamic response extends deep into the tissue as well as laterally across cortex, and involves considerable trial-to-trial variability (Drew *et al*, 2011). A full understanding of the response requires the ability to quantify flow from hundreds of vessels within a large volume of tissue. This represents an important challenge, as TPLSM is pushed to its limits in imaging depth (Helmchen and Denk, 2005; Kobat *et al*, 2009; Oheim *et al*, 2001; Theer *et al*, 2003; Theer and Denk, 2006) and line scanning speed (Göbel and Helmchen, 2007; Göbel *et al*, 2007; Lillis *et al*, 2008; Valmianski *et al*, 2010). Currently with TPLSM, long imaging sessions are needed to measure over a large population of distantly located vessels, and measurements would not be obtained simultaneously. Even with the user-defined line scan capability demonstrated here (Figure 4), the imaging of cellular activity and vascular response is limited to closely associated cells and vessels that lie in the same imaging plane. New tools that enable rapid shifting of the focal plane could extend the capability of the techniques discussed here. These include: (i) pairs of acousto-optic deflectors to both scan the laser beam in the *x*, *y* plane, and also adjust the beam divergence to enable *z* axis scanning (Mermillod-Blondin *et al*, 2008; Olivier *et al*, 2009) and (ii) acoustically modulated gradient refractive index lenses (Reddy and Saggau, 2005; Reddy *et al*, 2008; Salome *et al*, 2006). These approaches could enable the construction of complex, three-dimensional line scan patterns that sample the activity of hundreds of cells and vessel segments (of any orientation) throughout a cortical column near simultaneously. Thus far, these techniques have been used primarily for $[Ca^{2+}]_{int}$ and voltage-sensitive dye imaging, but should be amenable to blood flow imaging.

Although not permitting the true three-dimensional line scanning just described, techniques to more slowly shift the focal plane with piezoelectrically actuated microscope objective mounts (Göbel *et al*, 2007), or to sample multiple focal planes simultaneously by multiplexing the imaging beam (Carriles *et al*, 2008; Cheng *et al*, 2011) offer the

capability to acquire data at multiple cortical depths in rapid succession. Further, evolving techniques such as Doppler optical coherence microscopy (Srinivasan *et al*, 2011) and photoacoustic microscopy (Hu and Wang, 2010), may become more suitable for studying the hemodynamic process over broader areas of cortex while maintaining single vessel resolution.

Limitations to imaging of deep structures in cortex may be overcome with longer wavelength and improved photon collection (Kobat *et al*, 2009), or the use of microprisms (Levene *et al*, 2004). However, observation of flow in white matter and subcortical structures, which lie more than 1 mm below the brain surface in mice, require the removal of a column of cortical tissue (Dombeck *et al*, 2010). Microendoscopic methods using GRIN lenses allow stable imaging for weeks after the placement of a glass guide cannula through the cortex (Barretto *et al*, 2009). This approach would be of particular interested when studying small vessel diseases that afflict deeper brain structures, such as subcortical lacunar stroke and leukoariosis.

Acknowledgements

The authors thank to Pablo Blinder, David A Boas, Timothy H Murphy, Sava Sakadžiæ and Serge Chapak for generously contributing artwork and images. We also thank Celine Mateo for critical reading of the manuscript.

Disclosure/conflict of interest

The authors declare no conflict of interest.

References

Airan RD, Thompson KR, Fenno LE, Bernstein H, Deisseroth K (2009) Temporally precise *in vivo* control of intracellular signaling. *Nat Methods* 458:1025–9

Akemann W, Mutoh H, Perron A, Rossier J, Knopfel T (2010) Imaging brain electric signals with genetically targeted voltage-sensitive fluorescent proteins. *Nat Methods* 7:643–9

Alexander GM, Rogan SC, Abbas AI, Armbruster BN, Pei Y, Allen JA, Nonneman RJ, Hartmann J, Moy SS, Nicolelis MA, McNamara JO, Roth BL (2009) Remote control of neuronal activity in transgenic mice expressing evolved G protein-coupled receptors. *Neuron* 63:27–39

Ances BM, Greenberg JH, Detre JA (1999) Laser doppler imaging of activation-flow coupling in the rat somatosensory cortex. *Neuroimage* 10:25–8

Attwell D, Buchan AM, Charpak S, Lauritzen M, MacVicar BA, Newman EA (2010) Glial and neuronal control of brain blood flow. *Nature* 468:232–43

Ayata C, Dunn AK, Gursoy-Ozdemir Y, Huang Z, Boas DA, Moskowitz MA (2004) Laser speckle flowmetry for the study of cerebrovascular physiology in normaland ischemic mouse cortex. *J Cereb Blood Flow Metab* 24:744–55

Babcock AM, Standing D, Bullshields K, Schwartz E, Paden CM, Poulsen DJ (2005) *in vivo* inhibition of hippocampal Ca2+/calmodulin-dependent protein kinase II by RNA interference. *Mol Ther* 11:899–905

Bar T (1980) The vascular system of the cerebral cortex. *Adv Anat Embryol Cell Biol* 59:1–62

Barretto RP, Messerschmidt B, Schnitzer MJ (2009) *In vivo* fluorescence imaging with high-resolution microlenses. *Nat Methods* 6:511–2

Blinder P, Shih AY, Rafie CA, Kleinfeld D (2010) Topological basis for the robust distribution of blood to rodent neocortex. *Proc Natl Acad Sci USA* 107:12670–5

Boyden ES, Zhang F, Bamberg E, Nagel G, Deisseroth K (2005) Millisecond-timescale, genetically targeted optical control of neural activity. *Nat Neurosci* 8:1263–8

Brown CE, Li P, Boyd JD, Delaney KR, Murphy TH (2007) Extensive turnover of dendritic spines and vascular remodeling in cortical tissues recovering from stroke. *J Neurosci* 27:4101–9

Butz GM, Davisson RL (2001) telemetric measurement of cardiovascular parameters. *Physiol Genomics* 5:89–97

Buxton RB, Wong EC, Frank LR (1998) Dynamics of blood flow and oxygenation changes during brain activation: the balloon model. *Magn Reson Med* 39:855–64

Carriles R, Sheetz KE, Hoover EE, Squier JA, Barzda V (2008) Simultaneous multifocal, multiphoton, photon counting microscopy. *Opt Express* 16:10364–71

Cauli B, Tong XK, Rancillac A, Serluca N, Lambolez B, Rossier J, Hamel E (2004) Cortical GABA interneurons in neurovascular coupling: relays for subcortical vasoactive pathways. *J Neurosci* 24:8940–9

Cetin A, Komai S, Eliava M, Seeburg PH, Osten P (2006) Stereotaxic gene delivery in the rodent brain. *Nat Protoc* 1:3166–73

Chaigneau E, Oheim M, Audinat E, Charpak S (2003) Two-photon imaging of capillary blood flow in olfactory bulb glomeruli. *Proc Natl Acad Sci USA* 100:13081–6

Chaigneau E, Tiret P, Lecoq J, Ducros M, Knöpfel T, Charpak S (2007) The relationship between blood flow and neuronal activity in the rodent olfactory bulb. *J Neurosci* 27:6452–60

Chattopadhyaya B, Cristo GD, Higashiyama H, Knott GW, Kuhlman SJ, Welker E, Huang ZJ (2004) Experience and activity-dependent maturation of perisomatic GABAergic innervation in primary visual cortex during a postnatal critical period. *J Neurosci* 24:9498–611

Chen B, Friedman B, Cheng Q, Tsai PS, Schim E, Kleinfeld D, Lyden PD (2009) Severe blood-brain barrier disruptions and surrounding tissue injury. *Stroke* 40:e666–74

Cheng A, Goncalves JT, Golshani P, Arisaka K, Portera-Cailliau C (2011) Simultaneous two-photon calcium imaging at different depths with spatiotemporal multiplexing. *Nat Methods* 8:139–42

Chow BY, Han X, Dobry AS, Qian X, Chuong AS, Li M, Henninger MA, Belfort GM, Lin Y, Monahan PE, Boyden ES (2010) High-performance genetically targetable optical neural silencing by light-driven proton pumps. *Nature* 463:98–102

Chuquet J, Hollender L, Nimchinsky EA (2007) High-resolution *in vivo* imaging of the neurovascular unit during spreading depression. *J Neurosci* 27:4036–44

Costa DL, Lehmann JR, Harold WM, Drew RT (1986) Transoral tracheal intubation of rodents using a fiber-optic laryngoscope. *Lab Anim Sci* 36:256–61

D'Hooge R, De Deyn PP (2001) Applications of the Morris water maze in the study of learning and memory. *Brain Res Brain Res Rev* 36:60–90

Dalkara T, Irikura K, Huang Z, Panahian N, Moskowitz MA (1995) Cerebrovascular responses under controlled and monitored physiological conditions in the anesthetized mouse. *J Cereb Blood Flow Metab* 15:631–8

Dancause N, Barbay S, Frost SB, Plautz EJ, Chen D, Zoubina EV, Stowe AM, Nudo RJ (2005) Extensive cortical rewiring after brain injury. *J Neurosci* 25:10167–79

Das RR, Seshadri S, Beiser AS, Kelly-Hayes M, Au R, Himali JJ, Kase CS, Benjamin EJ, Polak JF, O'Donnell CJ, Yoshita M, D'Agostino RB, DeCarli C, Wolf PA (2008) Prevalence and correlates of silent cerebral infarcts in the Framingham offspring study. *Stroke* 39:2929–35

Davalos D, Grutzendler J, Yang G, Kim JV, Zuo Y, Jung S, Littman DR, Dustin ML, Gan WB (2005) ATP mediates rapid microglial response to local brain injury *in vivo*. *Nat Neurosci* 8:752–8

Denk W, Strickler JH, Webb WW (1990) Two-photon laser scanning fluorescence microscopy. *Science* 248:73–6

Derdikman D, Hildesheim R, Ahissar E, Arieli A, Grinvald A (2003) Imaging spatiotemporal dynamics of surround inhibition in the barrels somatosensory cortex. *J Neurosci* 23:3100–5

Devor A, Hillman EM, Tian P, Waeber C, Teng IC, Ruvinskaya L, Shalinsky MH, Zhu H, Haslinger RH, Narayanan SN, Ulbert I, Dunn AK, Lo EH, Rosen BR, Dale AM, Kleinfeld D, Boas DA (2008) Stimulus-induced changes in blood flow and 2-deoxyglucose uptake dissociate in ipsilateral somatosensory cortex. *J Neurosci* 28:14347–57

Devor A, Sakadzic S, Saisan PA, Yaseen MA, Roussakis E, Srinivasan VJ, Vinogradov SA, Rosen BR, Buxton RB, Dale AM, Boas DA (2011) 'Overshoot' of O2 is required to maintain baseline tissue oxygenation at locations distal to blood vessels. *J Neurosci* 31:13676–81

Devor A, Tian P, Nishimura N, Teng IC, Hillman EM, Narayanan SN, Ulbert I, Boas DA, Kleinfeld D, Dale AM (2007) Suppressed neuronal activity and concurrent arteriolar vasoconstriction may explain negative blood oxygenation level-dependent signaling. *J Neurosci* 27:4452–9

Dirnagl U, Kaplan B, Jacewicz M, Pulsinelli W (1989) Continuous measurement of cerebral cortical blood flow by laser-Doppler flowmetry in a rat stroke model. *J Cereb Blood Flow Metab* 9:589–96

Dombeck DA, Graziano MS, Tank DW (2009) Functional clustering of neurons in motor cortex determined by cellular resolution imaging in awake behaving mice. *J Neurosci* 29:13751–60

Dombeck DA, Harvey CD, Tian L, Looger LL, Tank DW (2010) Functional imaging of hippocampal place cells at cellular resolution during virtual navigation. *Nat Neurosci* 13:1433–40

Dombeck DA, Khabbaz AN, Collman F, Adelman TL, Tank DW (2007) Imaging large-scale neural activity with cellular resolution in awake, mobile mice. *Neuron* 56:43–57

Drew PJ, Duyn JH, Galanov E, Kleinfeld D (2008) Finding coherence in spontaneous oscillations. *Nat Neurosci* 11:991–3

Drew PJ, Blinder P, Cauwenberghs G, Shih AY, Kleinfeld D (2010*a*) Rapid determination of particle velocity from space-time images using the Radon transform. *J Comput Neurosci* 29:5–11

Drew PJ, Shih AY, Driscoll JD, Knutsen PM, Davalos D, Blinder P, Akassoglou K, Tsai PS, Kleinfeld D (2010*b*) optical access through a polished and reinforced thinned skull. *Nat Methods* 7:981–4

Drew PJ, Shih AY, Kleinfeld D (2011) Fluctuating and sensory-induced vasodynamics in rodent cortex extends arteriole capacity. *Proc Natl Acad Sci USA* 108: 8473–8

Driscoll JD, Shih AY, Drew PJ, Kleinfeld D (2011*a*) Quantitative two-photon imaging of blood flow in cortex. In: *Imaging in neuroscience and development* Vol. 2 (Yuste R, ed), New York: Cold Spring Harbor Laboratory Press, 927–37

Driscoll JD, Shih AY, Iyengar S, Field JJ, White GA, Squire JA, Cauwenberghs G, Kleinfeld D (2011*b*) Photon counting, censor corrections, and lifetime imaging for improved detection in two-photon microscopy. *J Neurophysiol* 105:3106–13

Dunn AK, Bolay H, Moskowitz MA, Boas DA (2001) Dynamic imaging of cerebral blood flow using laser speckle. *J Cereb Blood Flow Metab* 21:195–201

Eikermann-Haerter K, Yuzawa I, Dilekoz E, Joutel A, Moskowitz MA, Ayata C (2011) Cerebral autosomal dominant arteriopathy with subcortical infarcts and leukoencephalopathy syndrome mutations increase susceptibility to spreading depression. *Ann Neurol* 69:413–8

Feng G, Mellor RH, Bernstein M, Keller-Peck C, Nguyen QT, Wallace M, Nerbonne JM, Lichtman JW, Sanes JR (2000) Imaging neuronal subsets in transgenic mice expressing multiple spectral variants of GFP. *Neuron* 28:41–51

Fernández-Klett F, Offenhauser N, Dirnagl U, Priller J, Lindauer U (2010) Pericytes in capillaries are contractile *in vivo*, but arterioles mediate functional hyperemia in the mouse brain. *Proc Natl Acad Sci USA* 107: 22290–5

Fiacco TA, Agulhon C, Taves SR, Petravicz J, Caspar KB, Dong X, Chen J, McCarthy KD (2007) Selective stimulation of astrocyte calcium *in situ* does not affect neuronal excitatory synaptic activity. *Neuron* 54:611–26

Filosa JA, Bonev AD, Nelson MT (2004) Calcium dynamics in cortical astrocytes and arterioles during neurovascular coupling. *Circ Res* 95:73–81

Finikova OS, Lebedev AY, Aprelev A, Troxler T, Gao F, Garnacho C, Muro S, Hochtrasser RM, Vinogradov SA (2008) Oxygen microscopy by two-photon-excited phosphorescence. *Chemphyschem* 9:1673–9

Flecknell PA (1987) *Laboratory animal anesthesia*. San Diego: Academic Press

Frostig RD, Lieke EE, Ts'o DY, Grinvald A (1990) Cortical functional architecture and local coupling between neuronal activity and the microcirculation revealed by *in vivo* high-resolution optical imaging of intrinsic signals. *Proc Natl Acad Sci USA* 87:6082–6

Garaschuk O, Milos RI, Konnerth A (2006) Targeted bulk-loading of fluorescent indicators for two-photon brain imaging *in vivo*. *Nat Protoc* 1:380–6

Gentet LJ, Avermann M, Matyas F, Staiger JF, Petersen CH (2010) Membrane potential dynamics of GABAergic neurons in the barrel cortex of behaving mice. *Neuron* 65:422–35

Ginsberg MD, Busto R (1989) Rodent models of cerebral ischemia. *Stroke* 20:1627–42

Girouard H, Iadecola C (2006) Neurovascular coupling in the normal brain and in hypertension, stroke, and Alzheimer disease. *J Appl Physiol* 100:318–35

Göbel W, Helmchen F (2007) New angles on neuronal dendrites *in vivo*. *J Neurophysiol* 98:3770–9

Göbel W, Kampa BM, Helmchen F (2007) Imaging cellular network dynamics in three dimensions using fast 3D laser scanning. *Nat Methods* 4:73–9

Golanov EV, Ruggiero DA, Reis DJ (2000) A brainstem area mediating cerebrovascular and EEG responses to hypoxic excitation of rostral ventrolateral medulla in rat. *J Physiol* 529:413–29

Gold G, Giannakopoulos P, Herrmann FR, Bouras C, Kovari E (2007) Identification of Alzheimer and vascular lesion thresholds for mixed dementia. *Brain* 130:2830–6

Gordon GRC, Choi HB, Rungta RL, Ellis-Davies GCR, MacVicar BA (2008) Brain metabolism dictates the polarity of astrocyte control over arterioles. *Nature* 456:745–50

Greenberg DS, Houweling AR, Kerr JN (2008) Population imaging of ongoing neuronal activity in the visual cortex of awake rats. *Nat Neurosci* 11:749–51

Grinvald A, Lieke EE, Frostig RD, Gilbert CD, Wiesel TN (1986) Functional architecture of cortex revealed by optical imaging of intrinsic signals. *Nature* 324:361–4

Hainsworth AH, Markus HS (2008) Do *in vivo* experimental models reflect human cerebral small vessel disease? A systematic review. *J Cereb Blood Flow Metab* 28: 1877–91

Hamel E (2006) Perivascular nerves and the regulation of cerebrovascular tone. *J Appl Physiol* 100:1059–64

Harkness JE, Wagner JE (1989) *Biology and husbandry*. 3rd ed. Philadelphia: Lea and Febiger

Helmchen F, Denk W (2005) Deep tissue two-photon microscopy. *Nat Methods* 2:932–40

Helmchen F, Kleinfeld D (2008) *In vivo* measurements of blood flow and glial cell function with two-photon laser scanning microscopy. *Methods Enzymol* 444:231–54

Hoffman WE, Edelman G, Kochs E, Werner C, Segil L, Albrecht RF (1991) Cerebral autoregulation in awake versus isoflurane-anesthetized rats. *Anesth analg* 73:753–7

Holtmaat A, Bonhoeffer T, Chow DK, Chuckowree J, De Paola V, Hofer SB, Hübener M, Keck T, Knott G, Lee WC, Mostany R, Mrsic-Flogel TD, Nedivi E, Portera-Cailliau C, Svoboda K, Trachtenberg JT, Wilbrecht L (2009) Long-term, high-resolution imaging in the mouse neocortex through a chronic cranial window. *Nat Prot* 4:1128–44

Hu S, Wang LV (2010) Photoacoustic imaging and characterization of the microvasculature. *J Biomed Opt* 15:011101

Hua R, Walz W (2006) The need for animal models in small-vessel brain disease. *Crit Rev Neurobiol* 18:5–11

Hudetz AG, Feher G, Weigle CGM, Knuese DE, Kampine JP (1995) Video microscopy of cerebrocortical capillary flow: response to hypotension and intracranial hypertension. *Am J Physiol* 268:H2202–10

Hutchinson EB, Stefanovic B, Koretsky AP, Silva AC (2006) Spatial flow-volume dissociation of the cerebral microcirculatory response to mild hypercapnia. *Neuroimage* 32:520–30

Hutson KA, Masterton RB (1986) The sensory contribution of a single vibrissa's cortical barrel. *J Neurophysiol* 56:1196–223

Iadecola C, Nedergaard M (2007) Glial regulation of the cerebral microvasculature. *Nat Neurosci* 10:1369–76

Ji G, Feldman ME, Deng KY, Greene KS, Wilson J, Lee JC, Johnston RC, Rishniw M, Tallini YN, Zhang J, Wier WG, Blaustein MP, Xin HB, Nakai J, Kotlikoff MI (2004) Ca2+-sensing transgenic mice: postsynaptic signaling in smooth muscle. *Journal of Biological Chemistry* 279:21461–8

Jukovskaya N, Tiret P, Lecoq J, Charpak S (2011) What does local functional hyperemia tell about local neuronal activation? *J Neurosci* 31:1579–82

Jung S, Aliberti A, Graemmel P, Sunshine MJ, Kreutzberg GW, Sher A, Littman DR (2000) Analysis of fractalkine receptor CX(3)CR1 function by targeted deletion and green fluorescent protein reporter gene insertion. *Mol Cell Biol* 20:4106–14

Karaki H, Ozaki H, Hori M, Mitsui-Saito M, Amano K, Harada K, Miyamoto S, Nakazawa H, Won KJ, Sato K (1997) Calcium movements, distribution, and functions in smooth muscle. *Pharmacol Rev* 49:157–230

Kasischke KA, Lambert EM, Panepento B, Sun A, Gelbard HA, Burgess RW, Foster TH, Nedergaard M (2011) Two-photon NADH imaging exposes boundaries of oxygen diffusion in cortical vascular supply regions. *J Cereb Blood Flow Metab* 31:68–81

Kerr JN, Greenberg D, Helmchen F (2005) Imaging input and output of neocortical networks *in vivo*. *Proc Natl Acad Sci USA* 102:14063–8

Kim T, Kim SG (2011) Temporal dynamics and spatial specificity of aterial and venous blood volume changes during visual stimulation: implication for BOLD quantification. *J Cereb Blood Flow Metab* 31: 1211–1222

Kim TN, Masamoto K, Fukada M, Vazquez A, Kim SG (2010) Frequency-dependent neural activity, CBF, and BOLD fMRI in somatosensory stimuli in isoflurane-anesthetized rats. *Neuroimage* 52:224–33

Kleinfeld D (2002) Cortical blood flow through individual capillaries in rat vibrissa S1 cortex: stimulus induced changes are comparable to underlying fluctuations in flow. In: *Brain activation and cerebral blood flow control* Vol. 892. (Tomita M, ed), Tokyo: Elsevier International Congress Series, 115–22

Kleinfeld D, Blinder P, Drew PJ, Driscoll JD, Muller A, Tsai PS, Shih AY (2011) A guide to delineate the logic of neurovascular signaling in the brain. *Front Neuroenergetics* 3:1–9

Kleinfeld D, Delaney KR (1996) Distributed representation of vibrissa movement in the upper layers of somatosensory cortex revealed with voltage sensitive dyes. *J Comp Neurol* 375:89–108

Kleinfeld D, Denk W (1999) Two-photon imaging of neocortical microcirculation. In: *Imaging neurons: a laboratory manual* (Yuste R, Lanni F, Konnerth A, eds), Cold Spring Harbor: Cold Spring Harbor Laboratory Press, 23.1–5

Kleinfeld D, Friedman B, Lyden PD, Shih AY (2008) Targeted occlusion to surface and deep vessels in neocortex via linear and nonlinear optical absorption. In: *Animal models of acute neurological injuries* (Chen J, Xu Z, Xu X-M, Zhang J, eds), Vol. 14. The Humana Press: New York, NY, pp 169–85

Kleinfeld D, Mitra PP (2011) Applications of spectral methods in functional brain imaging. In: *Imaging: a laboratory manual* Vol. 1. (Yuste R, ed), New York: Cold Spring Harbor Laboratory Press, 12.1–7

Kleinfeld D, Mitra PP, Helmchen F, Denk W (1998) Fluctuations and stimulus-induced changes in blood flow observed in individual capillaries in layers 2 through 4 of rat neocortex. *Proc Natl Acad Sci USA* 95:15741–6

Knutsen PM, Pietr M, Ahissar E (2006) Haptic object localization in the vibrissal system: behavior and performance. *J Neurosci* 26:8451–64

Ko KR, Ngai AC, Winn HR (1990) Role of adenosine in regulation of regional cerebral blood flow in sensory cortex. *Am J Physiol* 259:H1703–8

Kobat D, Durst ME, Nishimura N, Wong AW, Schaffer CB, Xu C (2009) Deep tissue multiphoton microscopy using longer wavelength excitation. *Opt Express* 17:13354–64

Komiyama T, Sato TR, O'Connor DH, Zhang YX, Huber D, Hooks BM, Gabitto M, Svoboda K (2010) Learning-related fine-scale specificity imaged in motor cortex circuits of behaving mice. *Nature* 464:1182–6

Kontos HA (1989) Validity of cerebral arterial blood flow calculations from velocity measurements. *Stroke* 20:1–3

Kövari E, Gold G, Herrmann FR, Canuto A, Hof PR, Bouras C, Giannakopoulos P (2007) Cortical microinfarcts and demyelination affect cognition in cases at high risk for dementia. *Neurology* 66:927–31

Kovari E, Gold G, Herrmann FR, Canuto A, Hof PR, Michel JP, Bouras C, Giannakopoulos P (2004) Cortical microinfarcts and demyelination significantly affect cognition in brain aging. *Stroke* 35:410–4

Krupa DJ, Matell MS, Brisben AJ, Oliveira LM, Nicolelis MAL (2001) Behavioral properties of the trigeminal somatosensory system in rats performing whisker-dependent tactile discriminations. *J Neurosci* 21:5752–63

Kuchibhotla KV, Lattarula CR, Hyman BT, Bacskai BJ (2009) Synchronous hyperactivity and intercellular calcium waves in astrocytes in Alzheimer mice. *Science* 323:1211–5

Kuhlman SJ, Huang JZ (2008) High-resolution labeling and functional manipulation of specific neuron types in mouse brain by cre-activated viral gene expression. *PLoS ONE* 3:1–11

Lassen NA, Christenson MS (1976) Physiology of cerebral blood flow. *Br J Anaesth* 48:719–34

Lecoq J, Paraleix A, Poussakis E, Ducros M, Houssen YG, Vinogradov SA, Charpak S (2011) Simultaneous two-photon imaging of oxygen and blood flow in deep cerebral vessels. *Nat Med* 17:893–8

Lecoq JL, Tiret P, Najac M, Sheperd GM, Greer CA, Charpak S (2009) Odor-evoked oxygen consumption by action potential and synaptic transmission in the olfactory bulb. *J Neurosci* 29:1424–33

Lee JH, Durand R, Gradinaru V, Zhang F, Goshen I, Kim DS, Fenno LE, Ramakrishnan C, Deisseroth K (2010) Global and local fMRI signals driven by neurons defined optogenetically by type and wiring. *Nature* 465:788–92

Lefer DJ, Lynch CD, Lapinski KC, Hutchins PM (1990) Enhanced vasomotion of cerebral arterioles in sponaneously hypertensive rats. *Microvasc Res* 39:129–39

Levasseur JE, Wei EP, Raper AJ, Kontos AA, Patterson JL (1975) Detailed description of a cranial window technique for acute and chronic experiments. *Stroke* 6:308–17

Levene MJ, Dombeck DA, Kasischke KA, Molloy RP, Webb WW (2004) *In vivo* multiphoton microscopy of deep brain tissue. *J Neurophysiol* 91:1908–12

Li X, Zima AV, Sheikh F, Blatter LA, Chen J (2005) Endothelin-1-induced arrhythmogenic Ca2+ signaling is abolished in atrial myocytes of inositol-1,4, 5-triphosphte(IP3)-receptor type 2-deficient mice. *Circ Res* 96:1274–81

Lillis KP, Eng A, White JA, Mertz J (2008) Two-photon imaging of spatially extended neuronal network dynamics with high temporal resolution. *J Neurosci Methods* 172:178–84

Lindauer U, Villringer A, Dirnagl U (1993) Characterization of CBF response to somatosensory stimulation: model and influence of anesthetics. *Am J Physiol* 264:H1223–8

Ma Y, Hu H, Berrebi AS, Mathers PH, Agmon A (2006) Distinct subtypes of somatostatin-containing neocortical interneurons revealed in transgenic mice. *J Neurosci* 26:5069–82

Maaswinkel H, Whishaw IQ (1999) Homing with locale, taxon, and dead reckoning strategies by foraging rats: Sensory hierarchy in spatial navigation. *Behav Brain Res* 99:143–52

Mace E, Montaldo G, Cohen I, Baulac M, Fink M, Tanter M (2011) Functional ultrasound imaging of the brain. *Nat Methods* 8:662–4

Madisen L, Zwingman TA, Sunkin SM, Oh SW, Zariwala HA, Gu H, Ng LL, Palmiter RD, Hawrylycz MJ, Jones AR, Lein ES, Zeng H (2010) A robust and high-throughput Cre reporting and characterization system for the whole mouse brain. *Nat Neurosci* 13:133–40

Mank M, Santos AF, Direnberger S, Mrsic-Flogel TD, Hofer SB, Stein V, Hendel T, Reiff DF, Levelt C, Borst A, Bonhoeffer T, Hübener M, Griesbeck O (2008) A genetically encoded calcium indicator for chronic *in vivo* two-photon imaging. *Nat Methods* 5:805–11

Marker DF, Tremblay ME, Lu SM, Majewska AK, Gelbard HA (2010) A thin-skull window technique for chronic two-photon *in vivo* imaging of murine microglia in models of neuroinflammation. *J Vis Exp* 19:e2059

Martin C, Martindale J, Berwick J, Mayhew J (2006) Investigating neural-hemodynamic coupling and the hemodynamic response function in the awake rat. *Neuroimage* 32:33–48

Mayhew JEW, Askew S, Zeng Y, Porrill J, Westby GWM, Redgrave P, Rector DM, Harper RM (1996) Cerebral vasomotion: 0.1 Hz oscillation in reflectance imaging of neural activity. *Neuroimage* 4:183–93

McCaslin AF, Chen BR, Radosevich AJ, Cauli B, Hillman EM (2010) *In vivo* 3D morphology of astrocyte-vasculature interactions in the somatosensory cortex: implications for neurovascular coupling. *J Cereb Blood Flow Metab* 31:795–806

McGuill MW, Rowan AN (1989) Biological effects of blood loss: implications for sampling volumes and techniques. *ILAR News* 31:5–20

Mehta SB, Whitmer D, Figueroa R, Williams BA, Kleinfeld D (2007) Active spatial perception in the vibrissa scanning sensorimotor system. *PLoS Biol* 5:309–22

Meng W, Ma J, Ayata C, Hara H, Huang PL, Fishman MC, Moskowitz MA (1996) Ach dilates pial arterioles in endothelial and neuronal NOS knockout mice but NO-dependent mechanisms. *Am J Physiol* 271:H1145–50

Mermillod-Blondin A, McLeod E, Arnold CB (2008) High-speed varifocal imaging with a tunable acoustic gradient index of refraction lens. *Opt Lett* 33:2146–8

Misgeld T, Kerschensteiner M (2006) *In vivo* imaging of the diseased nervous system. *Nat Rev Neurosci* 7:449–63

Mohajerani M, Aminoltejari K, Murphy TH (2011) Targeted mini-strokes produce changes in interhemispheric sensory signal processing that are indicative of disinhibition within minutes. *Proc Natl Acad Sci* 108: E183–91

Moldestad O, Karlsen P, Molden S, Storm JF (2009) Tracheotomy improves experiment success rate in mice during urethane anesthesia and sterotaxic surgery. *J Neurosc Methods* 176:57–62

Morii S, Ngai AC, Winn HR (1986) Reactivity of rat pial arterioles and venules to adenosine and carbon dioxide: with detailed description of the closed cranial window technique in rats. *J Cereb Blood Flow Metab* 6:34–41

Mostany R, Portera-Cailliau C (2008) A method for 2-photon imaging of blood flow in the neocortex through a cranial window. *J Vis Exp* 12:678

Mostany R, Portera-Cailliau C (2011) Absence of large-scale dendritic plasticity of layer 5 pyramidal neurons in peri-infarct cortex. *J Neurosci* 31:1734–8

Motoike T, Loughna S, Perens E, Roman BL, Liao W, Chau TC, Richardson CD, Kawate T, Kuno J, Weinstein BM, Stainer DY, Sato TN (2000) Universal GFP reporter for the study of vascular development. *Genesis* 28:75–81

Mulligan SJ, MacVicar BA (2004) Calcium transients in astrocyte endfeet cause cerebrovascular constrictions. *Nature* 431:195–9

Murphy PA, Lam MT, Wu X, Kim TN, Vartanian SM, Bollen AW, Carlson TR, Wang RA (2008*a*) Endothelial Notch4 signaling induces hallmarks of brain arteriovenous malformations in mice. *Proc Natl Acad Sci* 105:10901–6

Murphy TH, Li P, Betts K, Liu R (2008*b*) Two-photon imaging of stroke onset *in vivo* reveals that NMDA-receptor independent ischemic depolarization is the major cause of rapid reversible damage to dendrites and spines. *J Neurosc* 28:756–72

Ngai AC, Ko KR, Morii S, Winn HR (1988) Effect of sciatic nerve stimulation on pial arterioles in rats. *Am J Physiol* 254:H133–9

Ngai AC, Meno JR, Winn HR (1995) L-NNA suppresses cerebrovascular response and evoked potentials during somatosensory stimulation in rats. *Am J Physiol* 269:H1803–10

Nguyen J, Nishimura N, Fetcho R, Iadecola C, Schaffer CB (2011) Occlusion of cortical ascending venules causes blood flow decreases, reversals in flow direction, and vessel dilation in upstream capillaries. *J Cereb Blood Flow Metab* 31:2243–54

Nguyen Q-T, Tsai PS, Kleinfeld D (2006) MPScope: a versatile software suite for multiphoton microscopy. *J Neurosci Methods* 156:351–9

Nguyen Q-T, Dolnick EM, Driscoll J, Kleinfeld D (2009) MPScope 2.0: A computer system for two-photon laser scanning microscopy with concurrent plasma-mediated ablation and electrophysiology. In: *Methods for in vivo optical imaging* 2nd ed. (Frostig RD, ed), Boca Raton: CRC Press, 117–42

Nguyen Q-T, Schroeder LF, Mank M, Muller A, Taylor PW, Griesbeck O, Kleinfeld D (2010) An *in vivo* biosensor for neurotransmitter release and *in situ* receptor activity. *Nat Neurosci* 13:127–32

Niessing J, Ebisch B, Schmidt KE, Niessing M, Singer W, Galuske RA (2005) Hemodynamic signals correlate tightly with synchronized gamma oscillations. *Science* 309:948–51

Nimmerjahn A, Kirchhoff F, Kerr JN, Helmchen F (2004) Sulforhodamine 101 as a specific marker of astroglia in the neocortex *in vivo*. *Nat Methods* 29:31–7

Nir Y, Mukamel R, Dinstein I, Privman E, Harel M, Fisch L, Gelbard-Sagiv H, Kipervasser S, Fani A, Neufeld MY, Kramer U, Arieli A, Fried I, Malach R (2008) Interhemispheric correlations of slow spontaneous neuronal fluctuations revealed in human sensory cortex. *Nat Neurosci* 11:1100–8

Nishimura N, Rosidi NL, Iadecola C, Schaffer CB (2010) Limitations of collateral flow after occlusion of a single cortical penetrating arteriole. *J Cereb Blood Flow Metab* 30:1914–27

Nishimura N, Schaffer CB, Friedman B, Lyden PD, Kleinfeld D (2007) Penetrating arterioles are a bottleneck in the perfusion of neocortex. *Proc Natl Acad Sci USA* 104:365–70

Nishimura N, Schaffer CB, Friedman B, Tsai PS, Lyden PD, Kleinfeld D (2006) Targeted insult to individual subsurface cortical blood vessels using ultrashort laser pulses: three models of stroke. *Nat Methods* 3:99–108

Nolte C, Matyash M, Pivneva T, Schipke CG, Ohlemeyer C, Hanisch UK, Kirchhoff F, Kettenmann H (2001) GFAP promoter-controlled EGFP-expressing transgenic mice: a tool to visualize astrocytes and astrogliosis in living brain tissue. *Glia* 33:72–86

O'Connor DH, Clack NG, Huber D, Komiyama T, Myers EW, Svoboda K (2010) Vibrissa-based object localization in head-fixed mice. *J Neurosci* 30:1947–67

Ogawa S, Tank DW, Menon R, Ellermann JM, Kim S-G, Merkle H, Ugurbil K (1992) Intrinsic signal changes accompanying sensory stimulation: functional brain mapping with magnetic resonance imaging. *Proc Natl Acad Sci USA* 89:5951–5

Oheim M, Beaurepaire E, Chaigneau E, Mertz J, Charpak S (2001) Two-photon microscopy in brain tissue: parameters influencing the imaging depth. *J Neurosci Methods* 111:29–37

Okubo Y, Sekiya H, Namiki S, Sakamoto H, Iinuma S, Yamasaki M, Watanabe M, Hirose K, Iino M (2010) Imaging extrasynaptic glutamate dynamics in the brain. *Proc Natl Acad Sci USA* 107:6526–31

Oliva AA, Jr, Jiang M, Lam T, Smith TL, Swann JW (2000) Novel hippocampal interneuronal subtypes identified using transgenic mice that express green fluorescent protein in GABAergic interneurons. *J Neurosci* 20: 3354–68

Olivier N, Mermillod-Blondin A, Arnold CB, Beaurepaire E (2009) Two-photon microscopy with simultaneous standard and extended depth of field using a tunable acoustic gradient-index lens. *Opt Lett* 34:1684–6

Paxinos G, Watson C (1986) *The rat brain in stereotaxic coordinates*. San Diego: Academic Press

Peppiatt CM, Howarth C, Mobbs P, Attwell D (2006) Bidirectional control of CNS capillary diameter by pericytes. *Nature* 443:642–3

Petzold GC, Albeanu DF, Sato TF, Murthy VN (2008) Coupling of neural activity to blood flow in olfactory glomeruli is mediated by astrocytic pathways. *Neuron* 58:879–910

Ragan T, Sylvan JD, Kim KH, Huang H, Bahlmann K, Lee RT, So PT (2007) High-resolution whole organ imaging using two-photon tissue cytometry. *J Biomed Opt* 12:014015

Reddy GD, Kelleher K, Fink R, Saggau P (2008) Three-dimensional random access multiphoton microscopy for fast functional imaging of neuronal activity. *Nat Neurosci* 11:713–20

Reddy GD, Saggau P (2005) Fast three-dimensional laser scanning scheme using acousto-optic deflectors. *J Biomed Opt* 10:064038

Rosidi NL, Zhou J, Pattanaik S, Wang P, Jin W, Brophy M, Olbricht WL, Nishimura N, Schaffer CB (2011) Cortical microhemorrhages cause local inflammation but do not trigger widespread dendrite degeneration. *PLOS ONE* 6:e26612

Rovainen CM, Woolsey TA, Blocher NC, Wang D-B, Robinson OF (1993) Blood flow in single surface arterioles and venules on the mouse somatosensory cortex measured with videomicroscopy, fluorescent dextrans, nonoccluding fluorescent beads, and computer-assisted image analysis. *J Cereb Blood Flow Metab* 13:359–71

Roy CS, Sherington CS (1890) On the regulation of the blood supply of the brain. *J Physiol* 11:85–108

Roussakis E, Yaseen MA, Mandeville ET, Srinivasan VJ, Arai K, Ruvinskaya S, Devor A, Lo EH, Vinogradov SA, Boas DA (2010) Two-photon high-resolution measurement of partial pressure of oxygen in cerebral vasculature and tissue. *Nat Methods* 7:755–9

Sakadzić S, Roussakis E, Yaseen MA, Mandeville ET, Srinivasan VJ, Arai K, Ruvinskaya S, Devor A, Lo EH, Vinogradov SA, Boas DA (2010) Two-photon high-resolution measurement of partial pressure of oxygen in cerebral vasculature and tissue. *Nature Methods* 7:755–9

Salome R, Kremer Y, Dieudonne S, Leger JF, Krichevsky O, Wyart C, Chatenay D, Bourdieu L (2006) Ultrafast random-access scanning in two-photon microscopy using acousto-optic deflectors. *J Neurosci Methods* 154:161–74

Sawinski J, Wallace DJ, Greenberg DS, Grossmann S, Denk W, Kerr JND (2009) Visually evoked activity in cortical cells imaged in freely moving animals. *Proc Natl Acad Sci USA* 106:19557–62

Schaffer CB, Friedman B, Nishimura N, Schroeder LF, Tsai PS, Ebner FF, Lyden PD, Kleinfeld D (2006) Two-photon imaging of cortical surface microvessels reveals a robust redistribution in blood flow after vascular occlusion. *PLoSci Biol* 4:258–70

Scremin OU (1995) Cerebral vascular system. In: *The rat nervous system* (Paxinos G, ed), 2nd ed. San Diego: Academic Press, Inc., 3–35

Secomb TW, Hsu R, Pries AR (1998) A model for red blood cell motion in glycocalyx-lined capillaries. *Am J Physiol* 274:H1016–22

Shigetomi E, Kracun S, Khakh BS (2010) Monitoring astrocyte calcium microdomains with improved membrane targeted GCaMP reporters. *Neuron Glia Biol* 6:183–91

Shih AY, Friedman B, Drew PJ, Tsai PS, Lyden PD, Kleinfeld D (2009) Active dilation of penetrating arterioles restores red blood cell flux to penumbral neocortex after focal stroke. *J Cereb Blood Flow Metab* 29:738–51

Shih AY, Mateo C, Drew PJ, Tsai PS, Kleinfeld D (2012) A polished and reinforced thinned skull window for long-termimaging of mouse cortex. *J Vis Exp*, e3742; doi: 10.3791/3742 (in press)

Short CE (1987) *Principles and practice of veterinary anesthesia*. Baltimore: Williams and Willisms

Sigler A, Mohajerani MH, Murphy TH (2009) Imaging rapid redistribution of sensory-evoked depolarization through existing cortical pathways after targeted stroke in mice. *Proc Natl Acad Sci USA* 106:11758–64

Sirotin YB, Das A (2008) Anticipatory haemodynamic signals in sensory cortex not predicted by local neuronal activity. *Nature* 457:475–9

Sohya K, Kameyama K, Yanagawa Y, Obata K, Tsumoto T (2007) GABAergic neurons are less selective to stimulus orientation than excitatory neurons in layer II/III of visual cortex, as revealed by *in vivo* functional Ca2+ imaging in transgenic mice. *J Neurosci* 27:2145–9

Srinivasan VJ, Atochin DN, Radhakrishnan H, Jiang JY, Ruvinskaya S, Wu W, Barry S, Cable AE, Ayata C, Huang PL, Boas DA (2011) Optical coherence tomography for the quantitative study of cerebrovascular physiology. *J Cereb Blood Flow Metab* 31:1339–45

Srinivasan VJ, adziæ S, Gorczynska I, Ruvinskaya S, Wu W, Fujimoto JG, Boas DA (2009) Depth-resolved microscopy of cortical hemodynamics with optical coherence tomography. *Opt Lett* 34:3086–8

Stefanovic B, Hutchinson E, Yakovleva V, Schram V, Russell JT, Belluscio L, Koretsky AP, Silva AC (2007) Functional reactivity of cerebral capillaries. *J Cereb Blood Flow Metab* 28:961–72

Stosiek C, Garaschuk O, Holthoff K, Konnerth A (2003) *In vivo* two-photon calcium imaging of neuronal networks. *Proc Natl Acad Sci USA* 100:7319–24

Suter OC, Sunthorn T, Kraftsik R, Straubel J, Darekar P, Khalili K, Miklossy J (2002) Cerebral hypoperfusion generates cortical watershed microinfarcts in Alzheimer disease. *Stroke* 33:1986–92

Takano T, Tian GF, Peng W, Lou N, Libionka W, Han X, Nedergaard M (2006) Astrocyte-mediated control of cerebral blood flow. *Nat Neurosci* 9:260–7

Tamamaki N, Yanagawa T, Tomioka R, Miyazaki J, Obata K, Kaneko T (2003) Green fluorescent protein expression and colocalization with calretinin, parvalbumin, and somatostatin in the GAD67-GFP knock-in mouse. *J Comp Neurol* 40:60–79

Theer P, Hasan MT, Denk W (2003) Two-photon imaging to a depth of 1000 micrometers in living brains by use of a Ti:Al2O3 regenerative amplifier. *Opt Lett* 28:1022–4

Theer P, Denk W (2006) On the fundamental imaging-depth limit in two-photon microscopy. *J Opt Soc Am A Opt Image Sci Vis* 23:3139–50

Tian L, Hires SA, Mao T, Huber D, Chiappe ME, Chalasani SH, Petreanu L, Akerboom J, McKinney SA, Schreiter ER, Bargmann CI, Jayaraman V, Svoboda K, Looger LL (2009) Imaging neural activity in worms, flies and mice with improved GCaMP calcium indicators. *Nat Methods* 6:875–81

Tian P, Teng I, May LD, Kurz R, Lu K, Scadeng M, Hillman EM, De Crespigny AJ, D'Arceuil HE, Mandeville JB, Marota JJ, Rosen BR, Lui TT, Boas DA, Buxton RB, Dale AM, Devor A (2010) Cortical depth-specific microvascular dilation underlies laminar differences in blood oxygenation level-dependendent functional MRI signal. *Proc Natl Acad Sci* 107:15246–51

Tiret P, Chaigneau E, Lecoq J, Charpak S (2009) Two-photon imaging of capillary blood flow in olfactory bulb glomeruli. *Methods Mol Biol* 489:81–91

Tsai PS, Blinder P, Kaufhold JP, Squier JD, Kleinfeld D (2011) All-optical, *in situ* histology of brain tissue with ultra-short laser pulses. In: *Imaging in neuroscience and development*, Vol. 2. New York: Cold Spring Harbor Laboratory Press, 437–46

Tsai PS, Friedman B, Ifarraguerri AI, Thompson BD, Lev-Ram V, Schaffer CB, Xiong Q, Tsien RY, Squier JA, Kleinfeld D (2003) All-optical histology using ultrashort laser pulses. *Neuron* 39:27–41

Tsai PS, Kaufhold J, Blinder P, Friedman B, Drew P, Karten HJ, Lyden PD, Kleinfeld D (2009) Correlations of neuronal and microvascular densities in murine cortex revealed by direct counting and colocalization of cell nuclei and microvessels. *J Neurosci* 18:14553–70

Tsai PS, Kleinfeld D (2009) *In vivo* two-photon laser scanning microscopy with concurrent plasma-mediated ablation: principles and hardware realization. In: *Methods for in vivo optical imaging* 2nd ed. (Frostig RD, ed), Boca Raton: CRC Press, 59–115

Tuor U, Simone CS, Barks JD, Post M (1993) Dexamethasone prevents cerebral infarction without affecting cerebral blood flow in neonatal rats. *Stroke* 24: 452–7

Valmianski I, Shih AY, Driscoll J, Matthews DM, Freund Y, Kleinfeld D (2010) Automatic identification of fluorescently labeled brain cells for rapid functional imaging. *J Neurophysiol* 104:1803–11

Vetri F, Menicucci D, Lapi D, Gemignani A, Colantuoni A (2007) Pial arteriolar vasomotion changes during cortical activation in rats. *Neuroimage* 38:25–33

Villringer A, Haberl RL, Dirnagl U, Anneser F, Verst M, Einhaupl KM (1989) Confocal laser microscopy to study microcirculation on the rat brain surface *in vivo*. *Brain Res* 504:159–60

Wang X, Lou N, Xu Q, Tian GF, Peng WG, Han X, Kang J, Takano T, Nedergaard M (2006) Astrocytic calcium signaling evoked by sensory stimulation *in vivo*. *Nat Neurosci* 9:816–23

Watson BD, Dietrich WD, Busto R, Wachtel MS, Ginsberg MD (1985) Induction of reproducible brain infarction by photochemically initiated thrombosis. *Ann Neurol* 17:497–504

Waynforth HB, Flecknell PA (1992) *Experimental and surgical techniques in the rat*. San Diego: Academic Press

Winship IR, Murphy TH (2008) *In vivo* calcium imaging reveals functional rewiring of single somatosensory neurons after stroke. *J Neurosci* 28:6592–606

Winship IR, Plaa N, Murphy TH (2007) Rapid astrocyte calcium signals correlate with neuronal activity and onset of the hemodynamic response *in vivo*. *J Neurosci* 27:6268–72

Woolsey TA, Rovainen CM, Cox SB, Henger MH, Liange GE, Liu D, Moskalenko YE, Sui J, Wei L (1996) Neuronal units linked to microvascular modules in cerebral cortex: response elements for imaging the brain. *Cereb Cortex* 6:647–60

Xin HB, Deng KY, Rishniw M, Ji G, Kotlikoff MI (2002) Smooth muscle expression of Cre recombinase and eGFP in transgenic mice. *Physiol Genomics* 10: 211–9

Yang G, Pan F, Parkhurst CN, Grutzendler J, Gan WB (2010) Thinned-skull cranial window technique for long-termimaging of the cortex in live mice. *Nat Protoc* 5:201–8

Zhang F, Wang L-P, Brauner M, Liewald JF, Ka K, Watzke N, Wood PG, Bamberg E, Nagel G, Gottschalk A, Deisseroth K (2007) Multimodal fast optical interrogation of neural circuitry. *Nature* 446:633–41

Zhang S, Boyd J, Delaney KR, Murphy TH (2005) Rapid reversible changes in dendritic spine structure *in vivo* gated by the degree of ischemia. *J Neurosci* 25:5333–8

Zhang S, Murphy TH (2007) Imaging the impact of cortical microcirculation on synaptic structure and sensory-evoked hemodynamic responses *in vivo*. *PLoS Biol* 5:e119

Zhu X, Bergles DE, Nishiyama A (2008) NG2 cells generate both oligodendrocytes and gray matter astrocytes. *Development* 135:145–57

Zhuo L, Sun B, Zhang CL, Fine A, Chiu SY, Messing A (1997) Live astrocytes visualized by green fluorescent protein in transgenic mice. *Dev Biol* 187:36–42

Zonta M, Angulo MC, Gobbo S, Rosengarten B, Hossmann KA, Pozzan T, Carmignoto G (2003) Neuron-to-astrocyte signaling is central to the dynamic control of brain microcirculation. *Nat Neurosci* 6:43–50